Ghosting and its Recovery Mechanisms in Multilayer Amorphous Selenium X-ray Detectors

Farzin Manouchehri

A Thesis
in
The Department
of
Electrical and Computer Engineering

Presented in Partial Fulfillment of the Requirements
for the Degree of Master of Applied Science (Electrical Engineering) at
Concordia University
Montréal, Québec, Canada

September 2008

© Farzin Manouchehri, 2008

Library and Archives Canada

Published Heritage Branch

395 Wellington Street
Ottawa ON K1A 0N4
Canada

Bibliothèque et Archives Canada

Direction du Patrimoine de l'édition

395, rue Wellington
Ottawa ON K1A 0N4
Canada

Your file Votre référence
ISBN: 978-0-494-45312-4
Our file Notre référence
ISBN: 978-0-494-45312-4

NOTICE:
The author has granted a non-exclusive license allowing Library and Archives Canada to reproduce, publish, archive, preserve, conserve, communicate to the public by telecommunication or on the Internet, loan, distribute and sell theses worldwide, for commercial or non-commercial purposes, in microform, paper, electronic and/or any other formats.

The author retains copyright ownership and moral rights in this thesis. Neither the thesis nor substantial extracts from it may be printed or otherwise reproduced without the author's permission.

AVIS:
L'auteur a accordé une licence non exclusive permettant à la Bibliothèque et Archives Canada de reproduire, publier, archiver, sauvegarder, conserver, transmettre au public par télécommunication ou par l'Internet, prêter, distribuer et vendre des thèses partout dans le monde, à des fins commerciales ou autres, sur support microforme, papier, électronique et/ou autres formats.

L'auteur conserve la propriété du droit d'auteur et des droits moraux qui protège cette thèse. Ni la thèse ni des extraits substantiels de celle-ci ne doivent être imprimés ou autrement reproduits sans son autorisation.

In compliance with the Canadian Privacy Act some supporting forms may have been removed from this thesis.

While these forms may be included in the document page count, their removal does not represent any loss of content from the thesis.

Conformément à la loi canadienne sur la protection de la vie privée, quelques formulaires secondaires ont été enlevés de cette thèse.

Bien que ces formulaires aient inclus dans la pagination, il n'y aura aucun contenu manquant.

Canada

ABSTRACT

Ghosting and its Recovery Mechanisms in Multilayer Amorphous Selenium X-ray Detectors

Farzin Manouchehri

During the last 15 years, many efforts have been directed towards the development of digital detectors for X-ray imaging. Direct conversion stabilized amorphous Selenium (a-Se)-based X-ray image detection with an active matrix array is one of the most widely used approaches which can provide excellent X-ray images, and is commercially available for mammography and general radiography. However, the X-ray sensitivity of a-Se detectors used in these systems changes as a result of previous X-ray exposures. This change in sensitivity which creates ghosting is recoverable by resting the detector for several hours. In this work, the physics of ghosting and its recovery mechanisms in multilayer a-Se detectors are experimentally and theoretically investigated.

A numerical model is developed to study the time and exposure dependent X-ray sensitivity of multilayer a-Se X-ray imaging detectors on repeated X-ray exposures. This model considers accumulated trapped charges and their effects (trap filling, recombination, electric field profile, electric field dependent electron-hole pair creation energy), the carrier transport in the blocking layers, X-ray induced meta-stable deep trap center generations, and the effects of charge injection. The time dependent carrier detrapping and structural relaxation (recovery of meta-stable trap centers) are also considered. The continuity equations for both holes and electrons, trapping rate equations, and the Poisson's equation across the photoconductor for a step X-ray

exposure are simultaneously solved by the Backward Euler finite difference method. It is found that the sensitivity in a rested sample is recovered mainly by the carrier detrapping and the recombination of the injected carriers with the existing trapped carriers. The sensitivity is expected to recover almost fully by resting the sample longer than the recovery time constant of the meta-stable trap centers. The theoretical model agrees well with the experimental results.

To my loving parents
Jina & Houshang

ACKNOWLEDGMENTS

I would first like to thank my parents for their ongoing support that I will always be grateful.

I wish to extend my sincere appreciation to Dr. M. Zahangir Kabir for his tireless efforts and invaluable guidance in the advancement of my education and career. I am also indebted to Dr. Vijay Devabhaktuni and would like to express my great appreciation for his unfailing help and support during the course of this work.

I wish to acknowledge Dr. Olivier Tousignant from Anrad Corporation for many fruitful discussions and giving me opportunities of doing experiments in Anrad.

Finally I would like to thank my colleagues Asif Mahmood, Kaustubha Mendhurwar, Ahmad Zbeeb, Navid Arbabi, Mani Najmabadi, and Rajasekar Kakumani for their helpful suggestions.

TABLE OF CONTENTS

List of Figures......x

List of Tables......xiv

List of Abbreviations......xv

Chapter 1 Introduction......1

1.1 X-ray Imaging......1

1.2 Digital X-ray Imaging......1

1.3 Flat Panel Detectors......2

1.4 Indirect Conversion Detectors......3

1.5 Direct Conversion Detectors......3

1.6 Image Formation......6

1.7 Specific Requirements of X-ray Imaging Systems......6

1.8 Ideal X-ray Photoconductors......7

1.9 Motivations......10

1.10 Research Objectives......12

1.11 Thesis Outline......13

Chapter 2 Background Theories and a-Se Propertes......14

2.1 X-ray Interactions in Photoconductors......14

2.2 X-ray Sensitivity....18

2.3 Image Ghosting....20

2.4 Amorphous Selenium (a-Se)....20

Chapter 3 X-ray Sensitivity, Ghosting, and its Recovery in Multilayer a-Se.... 27

3.1 Trapping and Recombination Mechanisms in a-Se....27

3.2 Analytical X-ray Sensitivity Model....30

3.3 Dynamic X-ray Sensitivity Model....36

3.4 Theoretical Ghosting Model for Multilayer a-Se Detectors....38

3.5 Theoretical Ghosting Recovery Model for Multilayer a-Se Detectors....47

Chapter 4 Results and Discussions....49

4.1 Sensitivity Reduction and Ghosting....49

4.2 Ghosting Recovery (Experimental Research)....63

4.3 Ghosting Recovery (Theoretical Research)....71

Chapter 5 Conclusions, Contributions, and Future Work....75

5.1 Ghosting (Sensitivity Reduction)....75

5.2 Ghosting Recovery....77

5.3 Contributions....77

5.4 Suggestions and Future Work 78

References...80

LIST OF FIGURES

Figure 1.1 A direct conversion based square flat panel detector used for digital radiography (Courtesy of ANRAD Corp.)........ 4

Figure 1.2 A simplified schematic diagram of the cross-sectional structure of two pixels of the photo conductive self-scanned X-ray image detector [2]....... 5

Figure 1.3 A view of a multilayer detector. X-rays could be radiated either on the n or p layer for positively and negatively biased samples...........................12

Figure 2.1 (a) The X-ray photon interacts with an orbiting electron (Rayleigh scattering), (b) the X-ray photon interacts with an outer-shell electron and creates and electron of kinetic energy E″ (Compton scattering) [18].........15

Figure 2.2 When photoelectric phenomenon occurs, the whole energy of the incident X-ray photon is transferred to an electron which is released from the atom. An electron from the outer shell fills the vacancy in the inner shell which produces fluorescent X-ray [18]..16

Figure 2.3 The overall mass attenuation and energy absorption coefficient in a-Se vs. photon energy [19]..18

Figure 2.4 The schematic of a three-layer X-ray image detector biased with voltage V. The area of the top and bottom electrodes is A [2]...............................19

Figure 2.5 A shadow impression of a previously acquired image is detectable in subsequent uniform exposure. Ghosting is revealed as a reduction in pixel sensitivity in previously exposed areas and can only be seen with subsequent X-ray images..20

Figure 2.6 Experimentally measured density of state function for amorphous Selenium [20-22]...22

Figure 2.7 An illustration of the band gap of a photoconductor. Shallow and deep trap centers are shown for both electrons and holes.... 23

Figure 3.1 Hole and electron concentration profile due to X-ray photo-generation [51]..33

Figure 3.2 Schematic diagram illustrating a three-layer photoconductor sandwiched between two large area parallel plate electrodes used in the model. An

electron and a hole are generated at x' and are drifting under the influence of the electric field F'. Holes and electrons are trapped in n and p layers respectively right after applying H.V 40

Figure 3.3 The schematic of positively biased sample showing the sample status and generation within the dark-time. The generation is due to injection.. 44

Figure 3.4 The schematic of positively biased sample showing the virtual process of hole detrapping and re-trapping during the dark-time............47

Figure 3.5 Three different steps of ghosting recovery simulation, (i) reading the initial sensitivity by radiating test pulses, (ii) radiating ghost pulse, (iii) recovery process, radiating the test pulses............48

Figure 4.1 (a) Relative X-ray sensitivity vs. accumulated X-ray exposure for a positively biased *n-i-p* a-Se detector. The closed circles represent experimental data and the solid line represents the theoretical fit to the experimental data. (b) The electric distributions across the photoconductor for different cumulative X-ray exposures [57]............51

Figure 4.2 (a) Electric field profile for a positively biased intrinsic sample considering an effective recombination coefficient ($f = 0.25$), including holes detrapping during 2-min dark-time, Collection of detrapped holes in 1 sec, (b) the electric field of the *n-i-p* sample, including hole detrapping, the same conditions as Figure 4.2 (a)............ 52

Figure 4.3 A comparison of the normalized sensitivity in a monolayer based detector (previous model) [13] shown with dashed line, a *n-i-p* based detector without injection shown with dotted line, and present model shown with solid line (positively biased, present model) [57]............53

Figure 4.4 (a) The normalized hole concentration, and (b) the normalized electron concentration across the positively biased sample determined by the three most important phenomena i) EHP generation due to X-ray radiation, ii) charge injections, iii) charge detrapping............53

Figure 4.5 (a) Relative X-ray sensitivity versus cumulative X-ray exposure for a negatively biased *p-i-n* a-Se detector. The closed circles represent experimental data and the solid line represents the theoretical fit to the experimental data [57]. (b) The electric distributions across the photoconductor for different cumulative X-ray exposures [57]............54

Figure 4.6 (a) Electric field profile for a negatively biased intrinsic sample considering an effective recombination coefficient ($f = 0.3$), including holes detrapping during 2-min dark-time, Collection of detrapped holes in 1 sec, (b) the

electric field of the *p-i-n* sample, including hole detrapping, without charge injection......55

Figure 4.7 A comparison of the normalized sensitivity in a monolayer based detector (previous model) [13], and a *p-i-n* based detector (negatively biased, present model), the effect of dark current is also shown......56

Figure 4.8 (a) The normalized hole concentration, and (b) the normalized electron concentration across the negatively biased sample determined by the three most important phenomena i) EHP generation due to X-ray radiation, ii) charge injections, iii) charge detrapping......57

Figure 4.9 (a) Relative dark current density vs. time for positively biased sample, (*n-i-p* based sample), with the conditions set for Figure 4.1 (b) relative dark current vs. time for negatively biased sample, (*p-i-n* based sample), with the conditions set for Figure 4.5......58

Figure 4.10 (a) The relative sensitivity of a *n-i-p* based sample including charge injection and hole detrapping, collection of injected charges and detrapped holes is performed within 1 second during 2-min dark-time. (b) The electric field profile for the same sample......59

Figure 4.11 (a) The relative sensitivity of a *p-i-n* based sample including charge injection and hole detrapping, collection of injected charges and detrapped holes is performed within 1 second during 2-min dark-time. (b) The electric field profile for the same sample......60

Figure 4.12 (a) Relative dark current density vs. time for positively biased sample, (*n-i-p* based sample), with the conditions set for Figure 4.10 (b) relative dark current vs. time for negatively biased sample, (*p-i-n* based sample), with the conditions set for Figure 4.11......61

Figure 4.13 The effect of electric field on the level of ghosting, the more the electric field is the less the amount of ghosting will be, (a) positively biased sample, (b) negatively biased sample in which, $\mu_e \tau'_{0e} \approx 3.5 \times 10^{-6}$ cm^2/V and $\mu_h \tau'_{0h} \approx 9.6 \times 10^{-6}$ cm^2/V......62

Figure 4.14 The comparison of relative sensitivity between two different dark-times while other conditions are the same. Positively biased sample, (*n-i-p*), all the conditions are the same as Figure 4.12 except electric field and dark-time......63

Figure 4.15 A schematic of the setup utilized to do the ghosting recovery process. The sample is placed in the sample box. The sensitivity is measured through PC using *TCL*......64

Figure 4.16 Experimental result, F_0 = 6 V/μm. Ten test pulses are radiated before the ghost pulse is applied. With applying ghost pulses sensitivity does not decreases which can be due to the relatively high electric field..............66

Figure 4.17 Experimental result, F_0 = 3 V/μm. Ten test pulses are radiated before the ghost pulse is applied. With applying ghost pulses relative sensitivity decreases ~ 15%...67

Figure 4.18 Experimental result, F_0 = 5 V/μm. Five test pulses are radiated before the ghost pulse is applied. The Al filter is removed during the ghost pulse, (X ~ 15R). (The dark-time between each two test pulses is 2 minutes)..............68

Figure 4.19 Experimental result, F_0 = 5 V/μm. Twelve test pulses are radiated before the ghost pulse is applied. The ghost pulse dose is ~1 R.............................69

Figure 4.20 Experimental result, F_0 = 10 V/μm. Twelve test pulses are radiated before the ghost pulse is applied. The ghost pulse dose is ~1 R.............................70

Figure 4.21 Measuring initial sensitivity, applying ghost pulse, and recovery process are shown. In the recovery process the effect of different phenomenon on ghosting recovery is illustrated. A) Shows the effect of hole release on ghosting recovery. B) Shows the effect of hole and electron release. C) Shows the effect of injection plus charge release, and D) is the fit curve including release of new meta-stable deep trap centers. (a) F_0 = 5 V/μm, (b) F_0 = 10 V/μm...72

Figure 4.22 (a) The change in electric field across the photoconductor with time in ghosting recovery process. (b) relative dark current versus time for the conditions of Figure 4.21 (b)...74

LIST OF TABLES

Table 1.1 Specifications for different applications of digital X-ray imaging systems. kVp is the maximum kV value applied across the X-ray tube during exposure time, and the maximum energy of emitted X-ray photons is equal the kVp value. (These data are taken from Rowlands and Yorkston [3])..7

Table 2.1 Typical ranges of some important carrier properties in a-Se.....................24

Table 4.1 Characteristics of the *n-i-p* sample used in experimental investigations for ghosting recovery...65

Table 4.2 Characteristics of the *p-i-n* sample used in experimental investigations for ghosting recovery...69

LIST OF ABBREVIATIONS

a-Se	Amorphous Selenium
a-Si:H	Hydrogenated amorphous Silicon
ADC	Analog to digital converter
AMA	Active matrix array
AMFPI	Active matrix flat panel imager
CT	Computed tomography
EHP	Electron hole pair
FET	Field effect transistor
IVAP	Intimate valance alternate pair
keV	Kilo electron volt
kVp	Kilo volt peak
LP	Lone pair
MRI	Magnetic resonance imaging
PC	Personal computer
TCL	Tool command language
TFT	Thin film transistor
VAP	Valance alternate pair

Chapter 1

Introduction

1.1 X-ray Imaging

An X-ray (or Röntgen ray) is a form of electromagnetic radiation with the wavelength in the range of 10-0.01 nanometers corresponding to frequencies in the range of 30 PHz-30 EHz. X-ray is produced by accelerating electrons and colliding them with a metal target (*e.g. Tungsten*). An accelerated electron decelerates upon colliding the metal target and if it contains enough energy, it can knock out an electron from the inner shell of the metal atom. Consequently, electrons from higher energy levels can fill out the vacancy and as a result X-ray photons will be emitted. The discovery of X-ray approximately 100 years ago by Wilhelm Röntgen led very quickly to the development of radiology and medical imaging which is one of the best methods to medical diagnosis [1].

1.2 Digital X-ray Imaging

Digital technology has revolutionized our lives. We are collecting, processing, sending, analyzing, and using more and more information at a faster pace. Among all applications, medical imaging is not an exception, and among all methods of medical imaging, X-ray imaging is used more frequently than others. The two most important advantages of digital X-ray imaging are;

1) Image portability.
2) Improvement in image quality and dose utilization.

Many medical modalities, such as CT, MRI, and ultrasound are inherently digital. However, standard, X-ray radiography and fluoroscopy are still primarily based on analog technology of screen/film and the image intensifier.

Medical X-ray imaging has recently made advances in areas such as improved film and screens, reduced exposure rates and improved equipment, but still almost 65% of X-ray imaging is accomplished with film screen systems. In these systems, the cassettes are loaded with film and taken to the examination room then to the X-ray equipment and after exposure they are returned to the dark room for development before a final image can be viewed. This procedure is a time consuming method which can be hastened through a digital process [2]. Practical digital X-ray imaging is based on TFT AMFPI (Thin film transistor active matrix flat panel imagers).

1.3 Flat Panel Detectors

A flat panel X-ray image detector is a large area integrated circuit that is able to capture an X-ray image and convert it to a digital form. These flat panel detectors can replace X-ray film/screen cassettes of today, and hence provide a smooth transition to digital radiography.

The flat panel consists of many pixels. Each pixel acts as an individual detector which produces a certain amount of charge relative to the amount of radiation it receives. There are two most common approaches to convert X-ray photons to electric charges. In the first approach known as indirect conversion, a layer of phosphor is used to convert X-ray to visible light, and then this visible light will be converted to electric charges through a *pin* photodiode incorporated to each pixel. However, in the second approach known as

direct conversion a suitable photoconductor which is able to convert the incident X rays directly to charge in one step is utilized [3].

For both indirect and direct conversions, the image is constructed by the charges residing on the panel's pixels. These charges are simply read out by scanning the arrays row by row using the peripheral electronics and multiplexing the parallel columns to a serial digital signal. This signal is then transmitted to a computer for storage and display.

1.4 Indirect Conversion Detectors

Indirect conversion systems based on thin film transistor arrays are constructed by adding amorphous Silicon photodiode circuitry and a scintillator as the top layers of the thin film transistor array. The scintillator converts the absorbed X-ray photons into visible light photons which are proportional to the radiated X-ray energy. These visible light photons are then converted to the electric charges using photodiode circuitry. It is worth to say that each photodiode in this method represents one pixel. The electric charges at each pixel are finally read out by the peripheral electronic circuitry. There are two types of scintillators used in this approach, structured and unstructured scintillator. If an unstructured scintillator is used, the visible light can be spread out to the neighboring pixels which can reduce the spatial resolution. To relatively solve this problem, structured scintillator made of Cesium Iodide crystals, which are grown on the detector, are used [4].

1.5 Direct Conversion Detectors

Direct conversion stabilized amorphous Selenium based X-ray image detectors with an active matrix array is one of the most widely used approach which can provide excellent

X-ray images and are commercially available for mammography and general radiography, and are under consideration for use in fluoroscopy and portal imaging [5-7]. It has been found that a direct conversion system can provide images that are superior in quality compared to that of an indirect conversion system and is also easier and cheaper to manufacture due to their simple structure [8-9]. As mentioned before, the layers including photodiode and scintillator (used in indirect conversions) will be replaced by a photoconductor in direct conversion. A flat panel active matrix direct conversion X-ray image sensor using a-Se as a detector is shown in Figure 1.1.

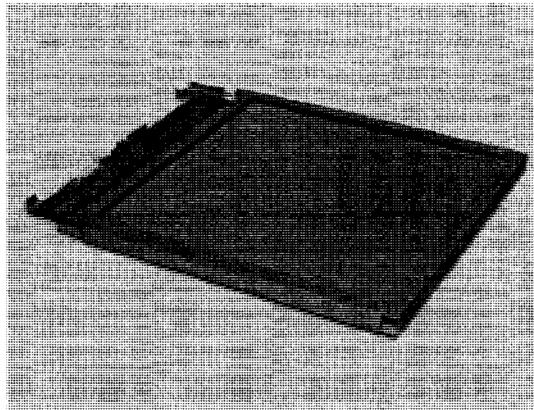

Figure 1.1 A direct conversion based square flat panel detector used for digital radiography (Courtesy of ANRAD Corp.).

A simplified schematic diagram of cross-sectional structure of two pixels of a-Se is shown in Figure 1.2. As can be seen in this figure, a photoconductor is sandwiched between two parallel plates representing the two electrodes. The top electrode is the radiation receiving electrode and the bottom electrode contains pixels collecting the electric charges. These collected charges will be stored on the pixel capacitors to form a latent image. A high voltage is applied between the two electrodes and consequently an electric field is provided within the detector. The electron hole pairs (EHPs) produced

due to X-ray photon absorption travel across the photoconductor and along the electric field lines. The radiation receiving electrode can be connected to either a positive or negative voltage with respect to the bottom electrode. Therefore, two types of detectors are defined; positively and negatively biased detectors respectively. Each of these detectors has its own characteristics and responses and is discussed in chapter 4.

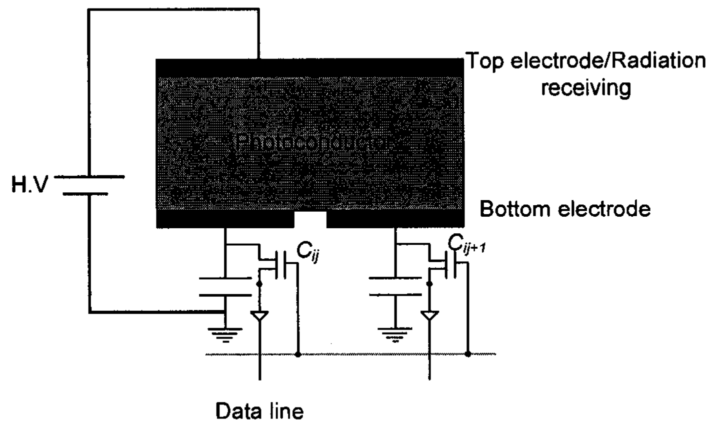

Figure 1.2 A simplified schematic diagram of the cross-sectional structure of two pixels of the photo conductive self-scanned X-ray image detector [2].

Each TFT has three electrical connections. The gate is to control the "on" or "off" state of the TFT; the drain is connected to the pixel electrode and the pixel storage capacitor (C_{ij}), which is made by overlapping the pixel electrode with either the adjacent gate line or a separate ground line; the source is connected to a common data line. A large band gap (> 2 eV), high atomic number semiconductor or X-ray photoconductor (*e.g.* stabilized amorphous Selenium, a-Se) layer is coated onto the active matrix array to serve as a photoconductor layer.

The capacitance of the photoconductor layer over the pixel is much smaller than the pixel capacitance C_{ij}, therefore, most of the applied voltage drops across the photoconductor.

To read out the latent image charge, Q_{ij}, the appropriate TFT is turned on every Δt seconds and the charge signal is transferred to the data line and hence to the charge amplifier. These signals are then multiplexed into serial data, digitized, and fed into a computer for imaging.

1.6 Image Formation

As mentioned before the most important difference between indirect and direct methods is that in direct method, X-ray photons are directly converted to electron hole pairs. Due to the application of an electric field across the detector, it can also be seen that charge transport is limited along vertical filed lines, significantly reducing lateral information spread. This phenomenon means that the output error in relation to the input radiation is minimized by the array resolution limited by the device geometry.

During the exposure time, the FET's are in the off mode while charge is collected at the signal storage capacitor. At the end of the exposure a positive pulse is applied to the FET gates starting with the first gate. The data lines connected to the FET source collect the charge from the drain. This charge is propagated to charge amplifiers connected to the data lines. The signals from the row are multiplexed and propagated to an ADC and stored in the computer memory. The readout process continues row by row [2].

1.7 Specific Requirements of X-ray Imaging Systems

Various medical systems such as chest radiology, mammography and fluoroscopy are designed based on certain specifications required for that application. Table 1.1 schemes the specifications for flat panel detectors for chest radiology, mammography and fluoroscopy

Table 1.1 Specifications for different applications of digital X-ray imaging systems. kVp is the maximum kV value applied across the X-ray tube during exposure time, and the maximum energy of emitted X-ray photons is equal the kVp value. (These data are taken from Rowlands and Yorkston [3]).

	Chest radiology	**Mammography**	**Fluoroscopy**
Detector size	35 cm × 43 cm	18 cm × 24 cm	25 cm × 25 cm
Pixel size	200 μm × 200 μm	50 μm × 50 μm	250 μm × 250 μm
Number of pixels	1750 × 2150	3600 × 4800	1000 × 1000
Readout time	~ 1 s	~ 1 s	~1/30 s
Spectrum	120 kVp	30 kVp	70 kVp
Average dose	300 μR	12 mR	1 μR
Radiation dose	30 – 3000 μR	0.6 – 240 mR	0.1 – 100 μR

1.8 Ideal X-ray Photoconductors

The photoconductor used in a digital X-ray image system is the core of the flat panel digital X-ray imager. Therefore, the selection and the fabrication process of the photoconductor can extremely affect the performance of the system. Consequently, it is necessary to identify some important characteristics of an ideal photoconductor in order to figure out the advantages and the disadvantages of the present model and finally to guide a search for developing the performance of the photoconductor. Some of the most important ideal characteristics of a photoconductor are as follows:

i) The photoconductor should absorb as many X-ray photons as possible within a practical thickness. This condition simply means that over the energy range of interest,

the absorption depth δ of the X-ray must be substantially less than the photoconductor thickness. Therefore, it is possible to avoid unnecessary patient exposure.

ii) The photoconductor must be able to generate as many EHPs as possible due to the X-ray radiation. It means that the amount of energy required to produce a single EHP, $W\pm$, must be as low as possible. Typically, $W\pm$ increases with the band gap Eg of the photoconductor.

iii) The diffusion of carriers should be negligible as compared to their drift. This property ensures less time for lateral carrier and leads to better spatial resolution.

iv) In an ideal photoconductor, there should be no bulk recombination among generated electrons and holes drifting to the electrodes. Bulk recombination is proportional to the product of the concentrations of holes and electrons. In the range of clinical exposures the bulk recombination is negligible due to the small signal of radiation. In this case obviously, Augur recombination is also negligible [10].

v) Deep trapping of carriers should be as low as possible for an ideal photoconductor. For both electron and hole, $\mu\tau'F$ (the schubweg) >> L, where μ is the drift mobility, τ' is the deep trapping time (lifetime), F is the electric field, and L is the detector thickness. The schubweg is the distance, a carrier drifts before it is deeply trapped and unavailable for conduction.

vi) Charge injection/Dark current through the electrodes into the photoconductor is a source of noise which should be as small as possible. This condition means that the contacts to the photoconductor should be non-injecting contacts and the thermal

generation of carriers due to defects or states in the band gap should be substantially small. The larger the band gap of a photoconductor is, the less the conductivity the photoconductor will have. The dark current should preferably not exceed ~10 – 1000 pA/cm^2, depending on the clinical applications [2]. This condition conflicts with the second condition mentioned above.

vii) The longest carrier transit time must be shorter than the access time of the pixel.

viii) The properties of the photoconductor should not change with repeated number of X-ray exposures. Being exposed by the X-ray, some properties of the photoconductor are undermined.

ix) The photoconductor layer should be coated easily and cheaply onto a large area AMA circuit without damaging the electronic circuits. For instance, annealing the photoconductor material at temperatures above 300°C can damage the a-Si:H TFTs in the AMA panel. A large area detector is necessary in diagnostic radiography applications because there is no practical way of focusing X-ray radiation.

x) The temporal artifacts such as ghosting (the reduction in the detector sensitivity) should be as small as possible (ghosting mechanism is explained in Chapter 2).

The large area coating in areas typically 30 cm × 30 cm or greater, rules out the use of X-ray sensitive crystalline semiconductors, which are difficult to grow in such large areas. Thus, only amorphous or polycrystalline (poly) photoconductors are currently practical for use in large area X-ray image detectors. Amorphous Selenium (a-Se) is one of the most highly developed photoconductors for large area detectors due to its commercial use as an electro-photographic photoreceptor [11]. In fact, the direct conversion flat panel

imaging technology has been made possible by the use of two key elemental amorphous semiconductors: a-Si:H (used for TFTs) and a-Se (used for photoconductor layer). Although their properties are different, both can be readily prepared in large areas, which is essential for an X-ray image sensor. Amorphous Selenium can be easily coated as thick films (*e.g.* 100-1000 μm) onto suitable substrates by conventional vacuum deposition techniques without the need to raise the substrate temperature beyond 60-70°C (well below the damaging temperature of the AMA, *e.g.* ~ 300°C for a-Si:H panels). Its amorphous state maintains uniform characteristics to very fine scales over large areas. Thus currently stabilized a-Se (a-Se alloyed with 0.2–0.5%As and doped with 10–40 ppm Cl) is the preferred choice for X-ray image sensors because it has an acceptable X-ray absorption coefficient, good charge transport properties for both holes and electrons and in addition, dark current in a-Se is much smaller than many competing polycrystalline detectors [2, 12].

1.9 Motivations

Among significant parameters used to describe the performance of a-Se based X-ray image detector, the sensitivity of the detector is one of the most critical ones especially the stability of sensitivity under repeated X-ray exposures (sensitivity is explained in chapter 2). It is found experimentally that the X-ray sensitivity of the detector decreases with subsequent exposures [13-15]. Change of sensitivity creates ghosting effect. A limited number of experiments have been done so far towards the study of change in the sensitivity of detectors [14-15]. As such, the change of sensitivity versus accumulated X-ray exposure and time, in a-Se based detectors, still remains an interesting research area. In addition to experimental studies, a few theoretical models have been proposed in order

to systematically study the change of sensitivity. The previous model by Kabir *et al.* [13] has many limitations. For instance, it is based on monolayer (intrinsic) a-Se detectors, while practical detectors are mostly based on multilayer a-Se detectors, and also they ignore the charge injection. Based upon these challenges in developing the theoretical and experimental study of change in sensitivity, the motivation of this work can be categorized as follows,

(i) Experimental study: A few experimental studies have been reported in literature to examine the sensitivity as a function of accumulated exposure [14-15], but there is no report of sensitivity recovery process. The study of change in detector sensitivity with repeated X-ray exposure and time, at different operating conditions could be instructive in order to improve the existing knowledge of this topic. The comparison of theoretical model with experimental data can explain the underlying mechanisms that cause ghosting and its recovery.

(ii) Modeling: As mentioned before, previous models are applicable for monolayer (intrinsic) a-Se based detectors. However, the practical detectors are made of multilayer structures, *e.g. p-i-n*. These models do not consider the effects of charge injection, whose importance is described in the latter chapter. For practical purposes, it is essential to use multilayer a-Se based detectors in order to decrease the amount of dark current [16-17]. Furthermore, the recovery process in a rested a-Se detector has not been theoretically modeled so far. This study is helpful to understand the reasons that are attributed to sensitivity fluctuations.

1.10 Research Objectives

The overall objectives of this thesis are: (i) to measure the sensitivity, ghosting and its recovery of multilayer a-Se based detectors under different operating conditions (*e.g.* applied biases) and on different samples, and (ii) to develop a theoretical model which is practical and consistent with reality.

In theoretical modeling part of this thesis, the previous model [13] is modified by incorporating carrier injection and carrier transport in blocking layers such that it can be applied to a multilayer a-Se detector.

Multilayer a-Se based sample refers to the three layers of *n*, *i* and *p*, mostly known as *n-i-p* samples in which *i* layer is sandwiched between *n* and *p* layers (*n* and *p* layers are commonly called blocking layers). Figure 1.3 illustrates a multilayer single X-ray detector. The specifications of *n*, *i*, and *p* layers will be discussed in chapter 3.

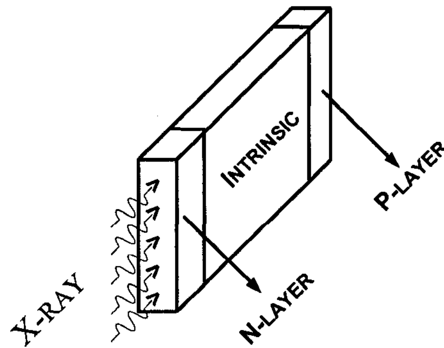

Figure 1.3 A view of a multilayer detector. X-rays could be radiated either on the *n* or *p* layer for positively and negatively biased samples.

Furthermore, the present model is capable of predicting the change of dark current versus time and includes carrier transport in all three layers. Including all these known effects into the theoretical model, it would be useful to compare the simulation results with

experimental data in order to study the cause of change in sensitivity versus accumulated exposure.

1.11 Thesis Outline

This thesis is divided into five chapters. Following the introduction chapter, a review of some useful theories of detectors and properties of a-Se is given in chapter two. The theoretical model and the details are given in chapter three. In chapter four, results and discussions are presented. Summary, contributions and recommended future work are presented in chapter five.

Chapter 2

Background Theories and a-Se Properties

In this chapter basic theories including X-ray interactions in photoconductor and X-ray image photoconductor specifications are discussed.

2.1 X-ray Interactions in Photoconductors

A portion of the incident X-ray is attenuated in the photoconductor layer of the detector. Attenuation is the removal of X-ray photons from the X-ray beam by either absorption or scattering events in the photoconductor layer. The fraction of the X-ray photons that are attenuated in the photoconductor layer is called the quantum efficiency η of the detector, and η is determined by the linear attenuation coefficient α cm^{-1} and the photoconductor thickness L as $\eta = 1 - e^{-\alpha L}$.

The energy of X-ray applicable to medical X-ray imaging varies from 10 keV to 120 keV. The X-ray interactions with a material can be divided into three different effects, which are *photoelectric* effect, *Rayleigh* scattering, and *Compton* scattering. The incident X-rays can be completely absorbed in the medium (*photoelectric* effect) or scattered (*Rayleigh* or *Compton* scattering).

Rayleigh scattering involves the elastic (coherent) scattering of X-rays by atomic electrons. The energy of the scattered X-ray remains the same as that of the incident X-

ray and there is no energy transfer from the X-ray to the medium. However, the scattered X-ray experiences a change in its path compared to that of the incident X-ray, and this change can undermine medical imaging, where the detection of scattered X-rays is undesirable.

Compton scattering involves an incoherent (inelastic) scattering of an X-ray photon by an atomic electron. *Compton* scattering usually happens when the energy of the X-ray photon is much greater than the binding energy of the atomic electron. Therefore, the *Compton* effect occurs with outer-shell of the atom, essentially free electrons in the medium. This interaction includes an electron of kinetic energy E'', an ionized atom, and a scattered X-ray photon of energy E' that is lower than the incident photon energy E. Therefore, some energy is transferred to the medium in *Compton* scattering phenomenon. The transferred energy depends on the scattering angle which is random. *Rayleigh* and *Compton* scattering phenomena are illustrated in Figure 2.1.

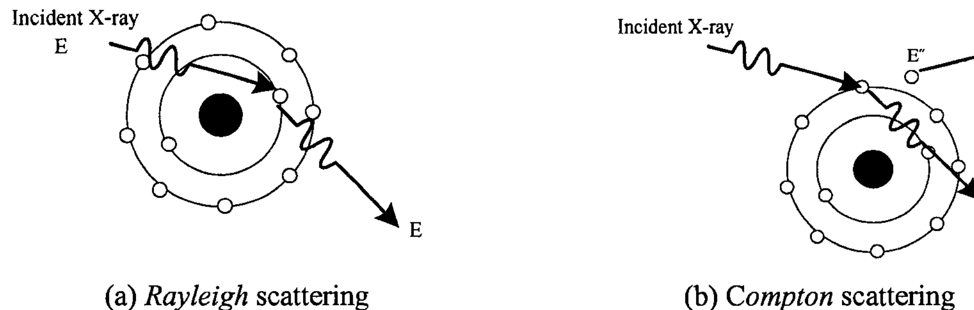

(a) *Rayleigh* scattering (b) *Compton* scattering

Figure 2.1 (a) The X-ray photon interacts with an orbiting electron (*Rayleigh* scattering), (b) the X-ray photon interacts with an outer-shell electron and creates and electron of kinetic energy E'' (*Compton* scattering) [18].

In the *photoelectric* interaction, the incident X-ray interacts with an electron in the medium, and the whole photon energy is transferred to the electron. Part of this energy is used to overcome the binding energy of the electron, and the remaining fraction becomes

the kinetic energy of the photoelectron. In this case the atom becomes ionized. If the energy of the incident X-ray is less than the binding energy of the electron, *photoelectric* interaction with that electron is not energetically feasible and hence will not occur. K-shell (the most inner shell) electrons are bound more tightly to the atom (higher binding energy) than outer-shell (L shell, M shell, and etc.) electrons. Thus, if *photoelectric* interaction is energetically unfeasible with K-shell electrons, interaction may still occur with an outer-shell electron. The binding energy associated with the K shell is called the K *edge* and so on for other shells. If an electron is released from an inner core shell, then a vacancy is replaced in its parent atom. Consequently, a cascade of electron transitions can occur, which can produce one or more *characteristics* X-rays (also called *fluorescent* X-rays) or alternately a series of non-radiative transitions involving *Auger* electrons will take place, resulting in the complete local deposition of energy through charged particles. The *characteristics* X-rays are named as K-fluorescent, L-fluorescent etc. based on the electron receiving shell. The *photoelectric* process is shown in Figure 2.2.

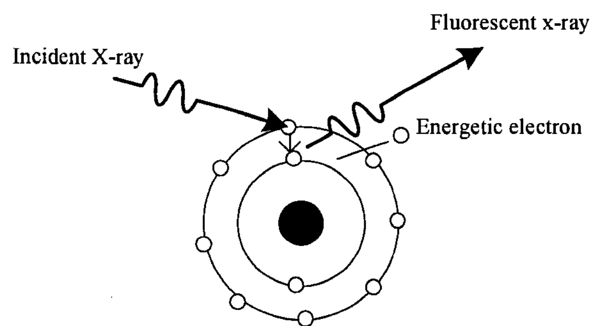

Figure 2.2 When *photoelectric* phenomenon occurs, the whole energy of the incident X-ray photon is transferred to an electron which is released from the atom. An electron from the outer shell fills the vacancy in the inner shell which produces fluorescent X-ray [18].

Energetic primary electrons created by *photoelectric* effect or *Compton* scattering travel in the solid, can cause ionization along its path and create many electron-hole pairs (EHPs). They can also interact with matter and produce *bremsstrahlung* radiation. When energetic electrons approach very close to the nucleus of the atom, they interact with the Coulomb field of the nucleus and orbit partially around the nucleus, and hence decelerate with the reduced energy. The loss in energy will appear as *bremsstrahlung* (breaking) radiation

Primary interaction of X-rays with the medium can be divided into two main categories. First, the creation of scattered photons including scattered X-rays through *Compton* or *Rayleigh* scattering events and the characteristics X-rays from *photoelectric* effect. Second, the creation of high energy photoelectrons by the *photoelectric* effect and the *Compton* scattering event. The high energy photoelectron transfers energy to the medium and hence creates EHPs, and also some of its energy can be lost by *bremsstrahlung* radiation. The entire process is random. However, the average energy absorbed in the medium by the primary X-ray interaction can be determined and is described by the energy absorption coefficient α_{en}. Thus, $(\alpha_{en}/\alpha)\,E$ is the average absorbed energy E_{ab} by primary X-ray interaction per attenuated X-ray photon of energy E. For a sample which is thick enough, the escaped radiations from the primary interaction can interact with atomic electrons of the medium like primary X-rays but at different points. Thus, the actual average absorbed energy per attenuated X-ray photon of energy E in a very thick detector is higher than $(\alpha_{en}/\alpha)\,E$.

The total mass attenuation and energy absorption coefficients of a-Se as a function of photon energy for diagnostics medical X-rays are shown in Figure 2.3. Figure 2.3 also

shows the individual contribution of photoelectric effect, *Rayleigh* and *Compton* scattering to the total attenuation. The mass attenuation (or energy absorption) coefficient of a material is the attenuation (or energy absorption) coefficient divided by its density. The *photoelectric* effect is the dominant interaction process in a-Se for diagnostics medical X-rays as shown in Figure 2.3. There is a sharp jump in the overall attenuation or energy absorption coefficient of a-Se at the photon energy of 12.66 keV (K-edge energy in a-Se) because of the onset of photoelectric interaction of X-rays with K-shell electrons.

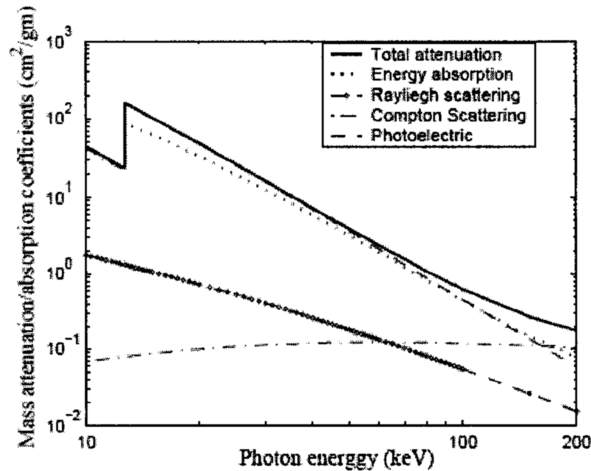

Figure 2.3 The overall mass attenuation and energy absorption coefficient in a-Se vs. photon energy [19].

2.2 X-ray Sensitivity

The X-ray sensitivity of an image detector is defined as the amount of collected charge per unit area per unit amount of exposure.

Sensitivity = $Q/(A\,.\,X)$, (2.1)

where Q is the collected charge in Coulomb (C), A is the radiation-receiving area in cm^2, and X is the amount of radiation in Roentgen (R). The unit of sensitivity is C cm^{-2} R^{-1}. One *Roentgen* is the quantity of radiation that creates ions carrying a total charge of

2.58×10^{-4} Coulombs per kg of air. It has been found that on average, it takes 33.97 eV to produce an ion pair in air. Thus the energy absorbed in one kilogram if air by a 1 R exposure is, 2.58×10^{-4} C/kg $\times$ 33.97 J/C = 0.00876 J/kg. The schematic diagram representing the equivalent circuit of a photoconductive detector is shown in Figure 2.4. A photoconductor layer is sandwiched between two large area parallel plate electrodes. A charge amplifier is connected to the pixel electrode (bottom electrode) and measures the collected charge by integrating the induced X-ray photocurrent through the pixel electrode (the integration time is longer than the exposure time). The radiation-receiving electrode (top electrode) is biased with a voltage V to establish an electric field F in the photoconductor. The biasing voltage can be positive or negative. The X-ray generated electrons and holes are drifted in opposite directions by the applied field and give rise to a transient X-ray photocurrent and the integration of the photocurrent is the collected charge.

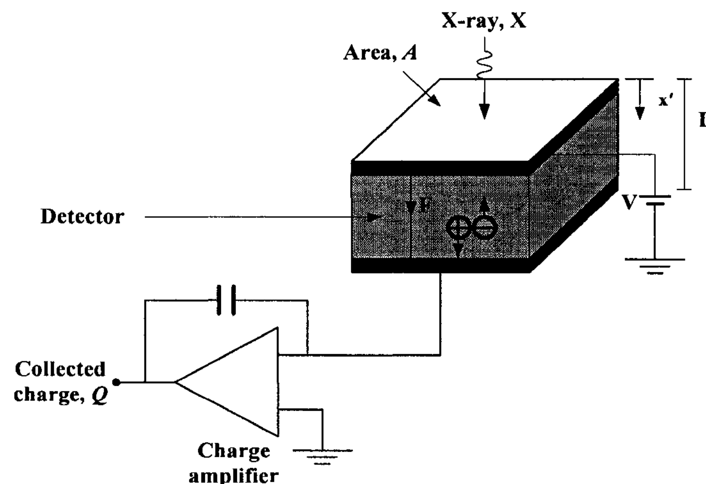

Figure 2.4 The schematic of a three-layer X-ray image detector biased with voltage V. The area of the top and bottom electrodes is A [2].

2.3 Image Ghosting

Ghosting phenomenon is the sensitivity reduction in an X-ray image detector due to the previous exposures. If a sample were under repeated X-ray exposures, it would record the effects of each previous exposure which is observable in the next exposures. As shown in Figure 2.5, a shadow impression of a previously acquired image is noticeable in subsequent uniform exposure. In this case, different areas have different sensitivities. In fact, ghosting is a phenomenon that can be seen only in subsequent exposures. Ghosting has also the potential to affect the X-ray image quality and this can be more severe while the images are produced at a faster pace compared to general radiography, *i.e.,* in fluoroscopy.

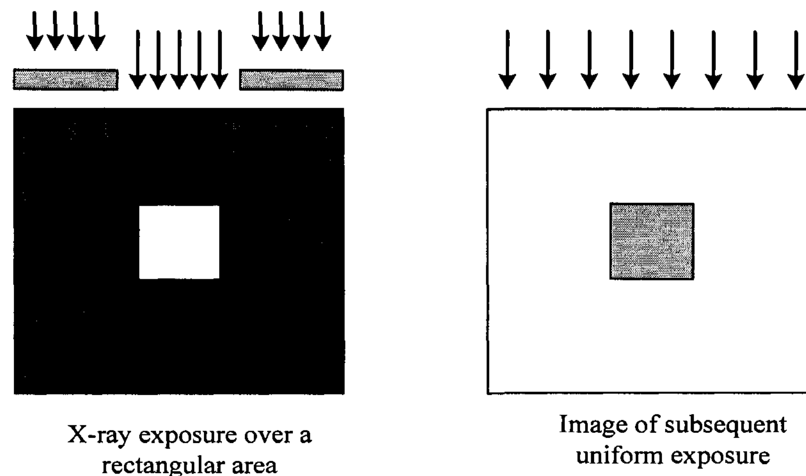

Figure 2.5 A shadow impression of a previously acquired image is detectable in subsequent uniform exposure. Ghosting is revealed as a reduction in pixel sensitivity in previously exposed areas and can only be seen with subsequent X-ray images.

2.4 Amorphous Selenium (a-Se)

Amorphous Selenium (a-Se) and its alloys have been well studied because of their importance in commercial xerography during the 1960s and 1970s. Amorphous Selenium

which is usually alloyed with 0.3% As, and doped with ppm level Cl is called stabilized amorphous Selenium and is presently a preferred material to be used as a photoconductor in X-ray medical image detectors. Stabilized a-Se, not pure a-Se, is used in the X-ray sensors, because pure a-Se is thermally unstable and crystallizes with time which varies from months to years depends on limited conditions [20]. It has been found that the rate of the crystallization can be reduced by alloying a-Se with small amount of As (0.2%-0.5%). Arsenic (As) atoms have a valency of III and so they are triply bonded and can link Se chains. Therefore, this characteristic can increase the viscosity of the amorphous structure. On the other hand, As can increase the amount of specific defects which act as hole traps and can decrease hole lifetime. The reduction in hole life time can be compensated for by adding a halogen (*e.g.* Cl) in the ppm level. The X-ray sensitivity of such a detector is related to the optical and electronic properties of the photoconductive a-Se layer. Therefore, a comprehensive understanding of the properties of a-Se is necessary in order to optimize the performance of these detectors. The density of a-Se is 4.3 g/cm^3, relative permittivity $\varepsilon_r = 6.7$, and energy gap $E_g \sim 2.22$ eV.

Selenium belongs to a set of elements called chalcogens which are located in the group VI column of periodic table. The atomic number of Selenium is 34, and there are twenty eight inner core electrons and six electrons in its valance band. Therefore, its atomic structure can be shown by [Ar] $4s^2 3d^{10} 4p^4$. The two electrons in the s-states along with an electron pair in one of the p-states do not participate in bonding and form a lone-pair (LP). The left two singly occupied p-states form covalent bonds with other atoms to form a solid. These two singly occupied p-states also split into bonding (B). In Se, the bond angle is about 105°. The currently known/accepted density of state model for a-Se is

shown in Figure 2.6. This model is developed using various measurements including both electro-photographic and photoconductivity experiments [20-22].

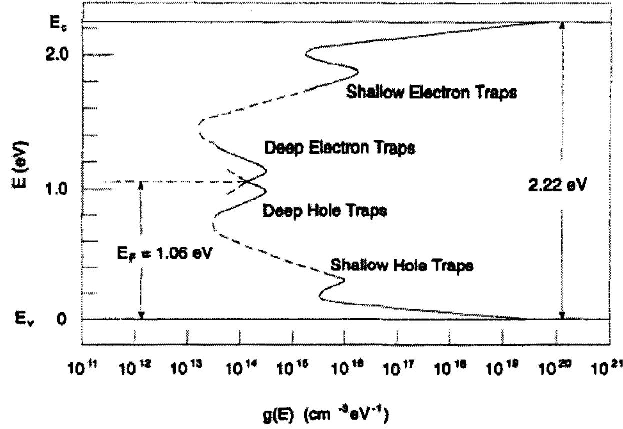

Figure 2.6 Experimentally measured density of state for amorphous Selenium [20-22]

There are many localized states in the so-called *forbidden gap* in a-Se. Some of these localized states are located near the band edges (*shallow traps*) and some of them are located deep in the energy band (*deep traps*). Various defects can cause localized states (both shallow and deep traps). These defects are stable at room temperature. Both shallow and deep trap centers can affect the movement of electrons and holes as shown in Figure 2.7 Deep traps can basically prevent charges from moving across the sample and shallow traps reduce charges' drift mobility. The effective mobility μ, can be defined as the mobility μ_0 in the extended states and is reduced by the trapping and release events due to the existence of shallow traps,

$$\mu = \frac{\tau_C}{\tau_C + \tau_r}\mu_0, \tag{2.2}$$

where τ_c and τ_r are the average capture and release times in shallow traps [20]. The capture time is defined as the mean time that takes a carrier to drift before it is trapped in shallow trap centers. In the same way the release time is the mean time that takes a

trapped carrier to be released from shallow trap centers. Thermal processes mostly dominate re-emissions from shallow trap centers. The drift mobilities in the extended states; the hole mobility $\mu_{0h} \approx 0.3$ cm^2/V-s and the electron mobility $\mu_{0e} \approx 0.1$ cm^2/V-s at room temperature [23-24]. The room-temperature effective hole mobility μ_h is independent of the preparation of the sample and has a value of ~ 0.12 cm^2/V-s whereas the effective electron mobility μ_e is in the range 0.003–0.006 cm^2/V-s [25].

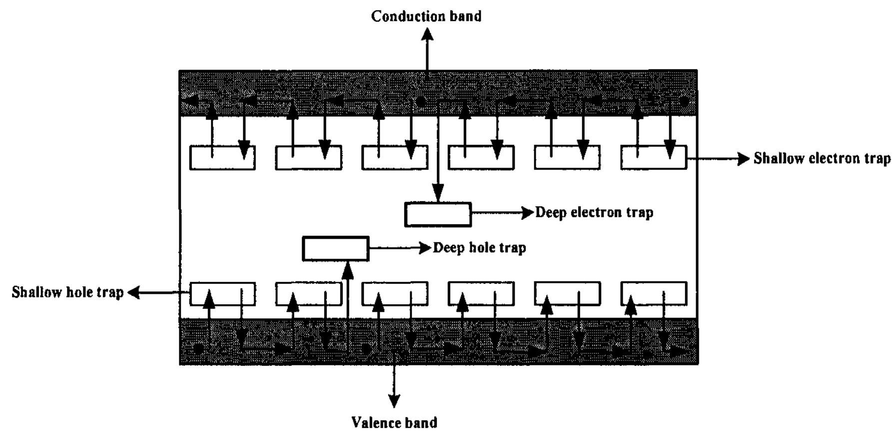

Figure 2.7 An illustration of the band gap of a photoconductor. Shallow and deep trap centers are shown for both electrons and holes.

Traveling across the photoconductor, carriers may experience many shallow trap and release phenomena because the release time due to the shallow trap is very short. Table 2.1 shows some common ranges of important properties of a-Se such as carrier mobilities and life-times.

Table 2.1 Typical ranges of some important carrier properties in a-Se

Property	Typical range
Hole mobility μ_h (cm^2/Vs)	0.12 - 0.14
Electron mobility μ_e (cm^2/Vs)	0.003 - 0.006
Hole lifetime τ_h (μs)	20 - 200
Electron lifetime τ_e (μs)	200 - 1000
Hole range $\mu_h\tau_h$ (cm^2/V)	2×10^{-6} - 2×10^{-5}
Electron range $\mu_e\tau_e$ (cm^2/V)	1×10^{-6} - 6×10^{-6}

As mentioned before, shallow traps reduce the mobility of carriers whereas deep traps prevent carriers from moving. Once a carrier is deeply trapped, it remains immobile until enough amount of energy, which is able to excite the trapped carrier back into the extended states, is transferred through a lattice vibration. Therefore, the carrier can drift again. The deep trap charge release time is very high. Consequently, once a carrier is deeply trapped, it is essentially removed from conduction, particularly under a high electric field applied across the sample. The high electric field causes the carrier transition time to be much less than carrier release time. As a result, the carrier life-time strongly depends on the concentration of deep trap centers rather than shallow trap centers. The charge life-time depends strongly upon the material, its impurities and preparation methods. For example, temperature of the a-Se substrate in the course of evaporation process can affect hole life-time. The less the substrate temperature is, the

less the hole life-time will be. Nevertheless, the electron life-time does not seem to be as much substrate-temperature dependent as holes. Increasing the concentration of As in a-Se decreases hole life-time, but increases electron life-time. In addition, the hole life-time increases significantly with adding Cl (chlorine) whereas the electron life-time decreases. Chlorine doping is more dominating in the sense of carrier ranges ($\mu\tau'$ product) than that of As doping. The typical ranges of electron and hole life-times are presented in Table 2.1. Taking deep trap capture coefficient $C_t \approx 10^{-8}$ cm^3 s^{-1}, and τ'_h = 50 μs, then the deep hole trap concentration is, $N_{0h} = \mu_{0h} / C_t \mu_h \tau'_h \approx 5 \times 10^{12}$ cm^{-3} [26].

The energy levels of hole and electron deep trap centers are about ~0.85 eV above the valence band and ~1 eV below the conduction band respectively [21, 27]. The carrier release times are related to the trap energy depth, E_t, by $v_0^{-1}\exp(E_t/KT)$, where K is Boltzmann constant, v_0 is phonon frequency, typically 10^{12} Hz, and T is the absolute temperature. Therefore, at room temperature the release times for electrons and holes are about few hours and less than 10 minutes. The release time-constant for shallow trapped holes is even less than 100 ns.

The EHP creation energy, $W_\pm$ strongly depends on the electric field but weakly depends on incident X-ray photon energy E [28-29]. The creation energy $W_\pm$ decreases with increasing electric field. In amorphous Selenium, the electron hole pair creation/generation energy follows an empirical relation given by [30],

$$W_\pm \approx W_\pm{}^0 + \frac{B(E)}{F^n}, \tag{2.3}$$

where $B(E)$ is the constant depending on the energy, $W_\pm{}^0$ is the saturated electron hole pair creation energy (when electric field is infinity), and n is normally 0.7 through 1 [31].

The energetic primary photon can create many EHPs, but only a fraction of the created electron hole pairs are collectable. This phenomenon means that a certain fraction of the created EHPs will be recombined before they can contribute to the photocurrent. There are two most important explanations of recombination process. The first explanation is called *Geminate* recombination (Gemini – The twins). In this type of recombination, the simultaneously generated electron and hole pairs are attracted to each other by Columbic force and may finally recombine. The second possible way is the recombination between *non-geminate* electrons and holes generated close to each other in the track of high energy electron created by an incident X-ray photon. This possible type of recombination is called *columnar* recombination. The fact is that in both cases, with increasing the field, which tries to separate the oppositely charges carriers, the amount of the charges which can escape from recombination should increase. If the field dependence of $W_{\pm}$ in a-Se is dominated by *geminate* or *columnar* recombination has not been fully determined and is presently a topical field of research [32]. Nevertheless, the energy dependence of $W_{\pm}$ is better understood. The overall change in creation energy from 20 keV to 6 MeV is of the factor of three. This fact appears to be due to a reduction of recombination with increase in energy.

The dark resistivity of a-Se is about 10^{14} Ω-cm. The dark current in a-Se photoconductors is less than the acceptable level (1 nA/cm^2) for an electric field as high as 20 V/μm. For *p-i-n* structure of a-Se detectors, dark current is less than 100 pA/cm^2 at fields as high as 20 V/μm [33].

Chapter 3

X-ray Sensitivity, Ghosting and its Recovery in Multilayer a-Se

In this chapter, following the analytical calculations of X-ray sensitivity of the detector, the dynamic ghosting and its recovery model are presented. However, before this, a brief discussion about trapping and recombination mechanisms in a-Se is necessary.

3.1 Trapping and Recombination Mechanisms in a-Se

It is well known that most of the deep trap centers in well-rested a-Se at room temperature are either positively or negatively charged [34-35]. The positive defects are the over-coordinated atoms of the type Se_3^+ (D^+). The negative defects are the under-coordinated atoms of the type Se_1^- (D^-). These two defects are called valence alternation pair (VAP). If the atoms of the pair (Se_3^+ and Se_1^-) are in close proximity, they are termed an intimate valence alternation pair (IVAP). The VAPs or IVAPs are thermodynamically derived structural defects, and the most native deep defects in a-Se are believed to be the IVAP types [34-35]. The IVAP centers and the overall structure of the material would appear neutral owing to the close proximity of positive and negative defects. Therefore, IVAPs act as low cross-sectional deep trapping centers rather than acting as high cross-sectional bimolecular recombination centers. Biegelson and Street

demonstrated that the most of the electrical and optical properties agree well with the IVAP model [35].

A single photogenerated hole can be captured by one IVAP (Se_3^+ and Se_1^-) and the IVAP transforms to the defect of the form (Se_3^+ and Se_1^0) [35]. Then, this defect (Se_3^+ and Se_1^0) turns into an exposed positively charged defect with higher cross-section [36], and may attract a drifting electron by coulombic attraction described by *Langevin* recombination process [37-38]. However, the Se_1^0 defect can release its captured hole by the thermal activation process and return to the Se_1^- state, thereby retaining the previous IVAP state. There is a possibility that Se_3^+ of the (Se_3^+ and Se_1^0) pair may interact with nearby Se_1^- to make an IVAP (Se_3^+ and Se_1^-), and Se_1^0 is separated from its initial pair. However, the Se_1^0 defect is unstable, and it can also lower its energy by utilizing LP electrons on neighbouring atoms for bonding. Consequently, Se_1^0 can be converted to Se_3^0 [34].

Similarly, a single photogenerated electron can be captured by one IVAP (Se_3^+ and Se_1^-) and creates (Se_3^0 and Se_1^-) defect. Then, this defect state (Se_3^0 and Se_1^-) turns into an exposed negatively charged defects with higher cross-section, and may attract a drifting hole by *Langevin* recombination process. There is a possibility that Se_1^- of the (Se_3^0 and Se_1^-) pair may interact with nearby Se_3^+ to make an IVAP (Se_3^+ and Se_1^-) and Se_3^0 is separated from its initial pair. The Se_3^0 defect is unstable, and can also be transferred to Se_3^+ and Se_1^- states [34], $2Se_3^0 \rightarrow Se_3^+ + Se_1^-$.

The above phenomenon suggests that only a certain fraction *f* of the trapped charges (or the exposed charged defect states) act as recombination centers for oppositely charged drifting carriers [39], and the returning of the meta-stable defect states (Se_3^0 or Se_1^0) to the IVAP defect states can be considered as the creation of deep trap centers.

One of the characteristic properties of an amorphous semiconductor is the existence of a wide range of effects when exposed to light. At room temperature, the incident light may create unstable neutral defect states Se_3^0 and Se_1^0 or meta-stable charged defect states Se_3^+ and Se_1^- [36, 40-41]. The unstable neutral defect states Se_3^0 and Se_1^0 may decay into the normal two-fold bond, or into a meta-stable VAP or IVAP [40]. Fritzsche [42] analysed all available evidences and concluded that illumination by light tends to induce atomic rearrangements and also VAP-like defects.

The creation of meta-stable deep trap centers in a-Se by X-rays has also been reported in the literature [43-44]. Recently, Rau *et al.* performed the hole X-ray time of flight (TOF) method to determine hole lifetime as a function of exposure or dose. They observed a monotonous decrease of hole lifetime, initially with a strong slope and with a smaller nearly linear slope at higher dose. The initial rapid drop in hole lifetime was attributed to the hole recombination with the trapped electrons, and the slow linear drop with dose suggested the generation of additional deep trap centers. Nesdoly [45] also performed a systematic study of X-ray induced changes in carrier transport properties in a-Se. The results suggested the creation of X-ray induced IVAP-like defects and that the concentration of IVAPs increases with increasing X-ray exposure or dose. It was also found that these IVAPs decay back to their equilibrium concentration within few hours. Since the amount of IVAPs in a rested sample is a thermodynamically derived value [46],

the atomic arrangements relax to their original states with time and the concentration of X-ray induced extra IVAPs decay to zero over time. Recently, the structural relaxation phenomenon in a-Se and its effects on the increase of carrier lifetimes have been reported by Allen *et al.* [47]. In their work, a ~15-20 hour structural relaxation time constant was observed.

3.2 Analytical X-ray Sensitivity Model

Some efforts have been made so far in order to study the change of the X-ray sensitivity of a photoconductor such as a-Se. Nemirovsky *et al.* [48] have studied charge collection efficiency based on exponential absorption of X-ray radiation. Kasap [31] has proposed a model for calculating X-ray sensitivity of a-Se detectors based on the consideration of exponentially decaying distribution of electron and hole pair (EHP) generation and distributed charge trapping effects across the photoconductor thickness. Kasap calculated the amount of collected charge in the external circuit for a mono-energetic X-ray beam by integrating the Hecht charge collection equation combined with X-ray attenuation profile. Kabir also analytically studied [49] the X-ray sensitivity of a-Se based detectors by solving the continuity equation, considering the drift of electrons and holes in the presence of deep traps under the situation of exponentially decaying distribution of electron-hole pair generation across the photoconductor thickness. An expression is derived for the amount of collected charge in terms of $W\pm$, X-ray exposure X, linear attenuation coefficient α and energy absorption coefficient α_{en} of the photoconductor, transport properties of the photoconductor (*i.e.,* carrier mobility μ, and carrier lifetime τ'), the operating conditions (*i.e.,* electric field F and X-ray photon energy E) and photoconductor thickness L. A generalized expression for charge carrier transport and

absorption-limited *normalized sensitivity* is also derived in terms of the following normalized parameters:

Δ = normalized attenuation depth (attenuation depth/thickness) = $1/(\alpha L)$,

τ_e = normalized electron schubweg (electron schubweg per unit thickness) = $\mu_e \tau'_e F/L$, and

τ_h = normalized hole schubweg (hole schubweg per unit thickness) = $\mu_h \tau'_h F/L$.

where $\mu_{e(h)}$ and $\tau'_{e(h)}$ are the mobility and deep trapping time (lifetime) of electrons (holes), respectively. Equivalently, τ_e and τ_h are the normalized carrier lifetimes (carrier lifetimes per unit transit time) for electrons and holes, respectively. When the charge collection and absorption-limited X-ray sensitivity is divided by the maximum sensitivity the normalized sensitivity will be obtained. Maximum sensitivity is the total collected charge if all the radiation is absorbed, then converted to charges which are all collected by the external circuit. The normalized sensitivity is determined by the X-ray absorption profile, photoconductor thickness and the charge collection efficiency, and closely controlled by Δ, τ_e and τ_h.

In this model, the following assumptions have been made to allow the problem to be analytically tractable. (1) The thermal equilibrium concentration of charge carriers is negligibly small. (2) The diffusion of carriers is negligible compared with their drift because of high applied field across the photoconductor. (3) A constant drift mobility μ and a single deep trapping time (lifetime) τ' are assigned to each type of carriers (holes and electrons) since the interrupted field time-of-flight measurements indicate a single deep trapping time for both types of carriers [31, 50]; the drifting carrier concentration falls exponentially as $\exp(-t'/\tau')$, where t' is the time. (4) The field remains relatively uniform. (5) The loss of carriers by deep trapping is more significant than bulk

recombination. (6) The trapped charge concentrations are very small compared to the trap center concentrations and thus trap saturation effect is negligible. (7) The photoconductor is exposed to a mono-energetic pulse of X-ray radiation that has a very short duration compared to the charge carrier transit times across the sample thickness. The assumptions (1) to (3) are the valid general assumptions for the photoconductors used in X-ray image detector for diagnostic medical applications. The assumptions (4) through (6) are valid for small signal operation (*e.g.* low carrier densities). In this case, there would be no interaction between drifting carriers. Since the detector system is linear by the assumptions (1) to (6), the assumption (7) can also be conveniently made to calculate X-ray sensitivity for small signal case.

The X-rays are attenuated exponentially as $\exp(-\alpha x')$ along the photoconductor thickness [31] and generate electron hole pair (EHP) concentration that follows the X-ray photon attenuation profile as shown in Figure 3.1. The X-ray generated carriers follow the straight electric field lines and either reach the electrodes or become trapped in the photoconductor. Figure 3.1 shows the hole and electron concentrations at the instant of carrier generation and also at a later time when the two distributions have drifted apart. It is assumed that the X-ray receiving electrode is biased positively. If the X-ray receiving electrode is negatively biased, then the electron and hole drifts have to be reversed. Neglecting the secondary photon interaction and taking Φ_0 as the number of X-ray photons per unit area, then, $\alpha_{en}\Phi_0 E\exp(-\alpha x')/W_{\pm}$ is the initial collectable hole or electron concentration at location x'. Note that the absorbed energy in the medium due to the secondary photon interaction is much less than the primary photon interaction. The secondary photon interaction is neglected in obtaining normalized sensitivity calculation

because it does not have any significant influence on the normalized sensitivity. As such, the initial hole or electron distribution across the medium is [51],

$$p'(x',0) = n'(x',0) = \frac{\alpha_{en} E \Phi_0}{w_{\pm}} \exp(-\alpha x') = B \exp(-\alpha x') \tag{3.1}$$

where B $(=\alpha_{en} E\Phi_0/W_{\pm})$ is the electron or hole concentration at location $x'= 0$ and time, $t' = 0$.

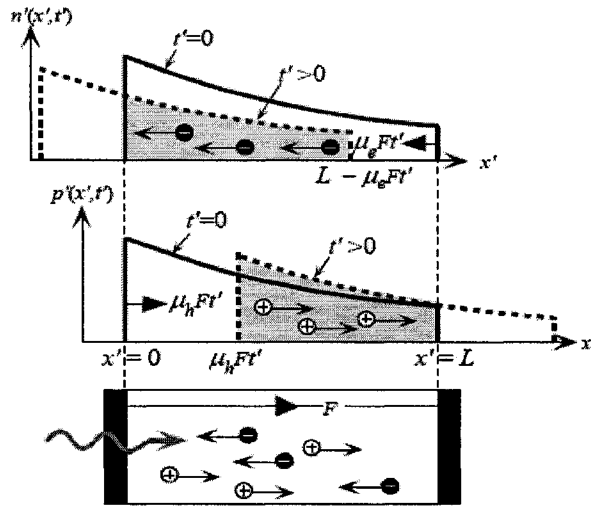

Figure 3.1 Hole and electron concentration profile due to X-ray photo-generation [51].

The incident X-ray photons per cm^2 is related to X-ray exposure X by,

$$\Phi_0 = \frac{0.00876 \times 10^{-3} X}{(\alpha_{air} / \rho_{air}) E}, \tag{3.2}$$

where X is in Roentgens, E is in eV, α_{air} and ρ_{air} are the energy absorption coefficient and the density of air respectively (α_{air}/ρ_{air} is in $cm^2 g^{-1}$) [18].

Considering the assumptions mentioned above, the continuity equation for holes under positive bias is given by,

$$\frac{\partial p'(x',t')}{\partial t'} = -\mu_h F \frac{\partial p'(x',t')}{\partial x'} - \frac{p'(x',t')}{\tau'_h}, \tag{3.3}$$

where $p'(x',t')$ is the concentration of holes at location x' at time t', and F is the applied field V/L [51].

The following normalized parameters for holes are introduced,

$$x = x'/L,\ t = t'/t_h,\ \tau_h = \tau'_h / t_h,\ \Delta = 1/(\alpha L), \text{ and } p = p'/p_0, \tag{3.4}$$

where $t_h = L/\mu_h F$ = transit time of the holes across the semiconductor. Thus, τ_h is the normalized hole lifetime (hole lifetime per unit transit time). Charge carrier concentrations are normalized with respect to the total collectable EHP generation in the photoconductor as if the total EHP is uniformly distributed over the sample volume. Therefore, the normalized parameter for hole concentration can be calculated as follows,

$$p_0 = n_0 = \frac{1}{L}\int_0^L B\exp(-\alpha x')dx' = B\Delta(1 - e^{-1/\Delta}) = B\Delta\eta, \tag{3.5}$$

where $\eta = 1 - \exp(-1/\Delta)$; quantum efficiency of the medium. The quantum efficiency represents that fraction of incident X-rays which interact with the detector [51].

Solving the normalized coordinates of equation (3.3), we can calculate the normalized collected electrons and holes.

The total collected charge is the sum of the collected charges due to holes and electrons. The total normalized collected charge, $Q = Q_h + Q_e$, which represents the *charge collection efficiency*. The normalized sensitivity s is the product of the normalized collected charge Q and the quantum efficiency η. Consequently,

$$S/S_0 = \tau_h[(1-e^{-\frac{1}{\Delta}}) + \frac{1}{\Delta/\tau_h - 1}(e^{-\frac{1}{\tau_h}} - e^{-\frac{1}{\Delta}})] + \tau_e[(1-e^{-\frac{1}{\Delta}}) - \frac{1}{\Delta/\tau e - 1}(1-e^{\frac{1}{\tau_e}-\frac{1}{\tau_e}})]$$

$$= s_{hole}(\tau_h, \Delta) + s_{electron}(\tau_e, \Delta) = s(\tau_h, \tau_e, \Delta), \quad (3.6)$$

where e is the elementary charge. If $W_\pm$ is in eV, α_{air}/ρ_{air} is in cm^2 g^{-1} and exposure is in Roentgens as in equation (3.2), then sensitivity is in C cm^{-2} R^{-1}. S_0 is a constant that depends on the X-ray photon energy and the material properties of the photoconductor since $W_\pm$ is a material property and can be taken as constant for a given material [52]. For those materials (*e.g.* a-Se) that have a field dependent $W_\pm$, then S_0 depends on the field [28-31]. The sensitivity S for a detector of finite thickness in which carrier collection is not perfect is always less than S_0.

The two square brackets on the right hand side of the normalized sensitivity s expression (equation 3.6) represent the relative contributions of hole and electron transport to the overall sensitivity for a given Δ. It is assumed that the radiation receiving side of the detector is biased positively. If the bias polarity is reversed, then τ_e and τ_h must be interchanged. The normalized sensitivity expression (3.6) takes into account only the charge transport and absorption effects. Note that $s(\tau_h, \tau_e, \Delta) = s_{hole} + s_{electron} = 1$ when all the incident radiation is absorbed and all the charges are collected, that is $\tau_h, \tau_e >> 1$ and $\Delta << 1$. The sensitivity then is simply S_0 and controlled by $W_\pm$.

3.3 Dynamic X-ray Sensitivity Model

Recent studies on a-Se based X-ray image detectors show that, the sensitivity of the photoconductor decreases with subsequent exposures [14, 53]. It is necessary to say that this reduction in the sensitivity because of accumulated exposures (known as ghosting) can be recovered and is reversible by some means such as letting the sample rest or shining light to the sample. The study of ghosting in a-Se based detectors has been a topical research area for several years because the exact reasons and the origins of this phenomenon have not been fully resolved. The reduction in sensitivity is usually shown as a function of exposure. Although the sensitivity reduction in a-Se photoconductor is not significantly large, the accurate studying and modeling of that would be important in order to characterize the photoconductor more precisely.

The recombination between X-ray photo-generated electrons and holes (*i.e.,* bimolecular recombination) can be neglected while the radiation is assumed to be as small signal, because the bulk recombination between drifting holes and electrons is strongly proportional to the product of the concentration of photo-generated holes and electrons.

The bulk carrier trapping has the following effects; i) due to each exposure, some of the carriers are trapped within the bulk of the photoconductor which can act as a capture centers for oppositely charged drifting carriers generated in the subsequent exposures. Therefore, the trapped carriers may recombine with the subsequently generated oppositely charged carriers leading to reduce charge collection efficiency. ii) As the number of exposures increases, the concentration of trapped carriers will increase which in turn can alter the electric field distribution across the photoconductor and hence change the EHP creation energy ($W_{\pm}$) in subsequent exposures. Considering these facts,

the X-ray sensitivity in the photoconductor is determined in each subsequent exposure. It is also reported that X-ray exposure can create new meta-stable deep trap centers which can reduce carrier lifetimes and sensitivity [54-56]. The release time of detrapped holes and electrons are in the range of several minutes and hours, respectively. Therefore, the amount of detrapped holes is significantly larger compared to the amount of detrapped electrons within a certain time.

It is worth to remind that, the model described in section 3.2 is an analytical model which is true for a rested sample in which there is no history of radiation. In order to be able to systematically study the change of sensitivity in a sample being exposed to accumulated X-ray radiation, a dynamic model which is capable of considering deep trapping of charge carriers, trapped charges due to the previous exposure, recombination between trapped charges and drifting carriers, electric field dependent electron-hole pair creation energy, detrapping of trapped carriers with time, and X-ray induced new meta-stable trap center generation must be taking into account.

Considering all the mentioned phenomena, Kabir studied the change of sensitivity (ghosting) for a monolayer a-Se sample [13]. The previous model [13] has the following drawbacks; (i) it is applicable to a single layer detector since it doesn't consider the effects of blocking layers on carrier generation and charge collection, (ii) it neglects the carrier injections from the metal electrodes and the collection of detrapped holes. These phenomena influence the trapped carrier distributions, electric field, and charge collection.

In this thesis however, the model is extended by considering three-layer photoconductor (known as *n-i-p* / *p-i-n* samples) instead of monolayer samples, and including effects of charge injection through electrodes into the blocking layers.

The objective of this chapter as the core of the thesis is:

To introduce the theoretical developed model based on three-layer a-Se detector including dark current contribution in charge collection efficiency and charge distributions across the photoconductor. The three layers across the detector are defined based on the specific characteristics of a-Se. The continuity equations for photo-generated and injected electrons and holes, trapping rate equations and poisson equation are solved simultaneously across the photoconductor by the finite difference method. The results are reported in chapter 4.

3.4 Theoretical Ghosting Model for Multilayer a-Se Detectors

Three-layer a-Se consists of three layers of *n*, *intrinsic*, and *p*. The definition of *n* and *p* layers is not the same as the conventional definition of these doped layers. The *p*- and *n*-layers (commonly called the blocking layers) are appropriately doped to serve as unipolar conducting layers that can easily trap electrons and holes, respectively, but allow the transport of oppositely charged carriers. The rate of emission of these deeply trapped carriers is so small that there is no significant current injection into the bulk of a-Se layer. This property means that the *p* and *n* layers have very high concentration of deep trap centers for electrons and holes respectively. In other words, the mobility-life time product ($\mu_{h(e)} \times \tau_{h(e)}$) of holes (electrons) in the *n*(*p*) layer is much less than that in the *intrinsic* layer while the mobility-life time product of holes (electrons) in the *p*(*n*) layer is assumed

to be the same as that in the *intrinsic* layer. The thin (a few microns) blocking layers start trapping charge carriers right after applying the bias field [57].

A multilayer photoconductor is sandwiched between two large area parallel plate electrodes and is biased with voltage V applied across the photoconductor. The photo-generated EHPs drift along the electric field lines. The diffusion of carriers is negligible compared to their drift because of the high applied electric field across the sample.

In ghosting measurement experiments, a series pulse of X-ray exposures is applied to the detector and the X-ray sensitivity of each X-ray exposure is measured. The exposure duration is typically 50-250 ms and there is a time gap (dark-time) of few minutes (typically 1 to 5 minutes) between two successive X-ray exposures. During the exposure, the rates of carrier injections due to dark current and carrier detrapping are much smaller than that of X-ray generated carriers. Therefore, the effects of dark current and carrier detrapping on the carrier dynamics during the exposure time are neglected. However, these effects are considered within the few minutes gap between two successive X-ray exposures [57]. Figure 3.2 shows serial X-ray pulses radiated to the sample with a dark-time of 1-5 minute(s) between each two successive exposures.

A constant drift mobility μ and a single deep trapping time (lifetime) τ' are assigned to each type of carrier (holes and electrons). The holes' (electrons') lifetimes in the intrinsic and p (n) layers are identical. As Figure 3.2 shows, during X-ray exposures, $p'(x', t')$ is defined as the free hole concentration, $n'(x', t')$ as the free electron concentration, $p'_t(x', t')$ as the trapped hole concentration, and $n'_t(x', t')$ as the trapped electron concentration at point x' at time t'. Therefore, following equations are true [13];

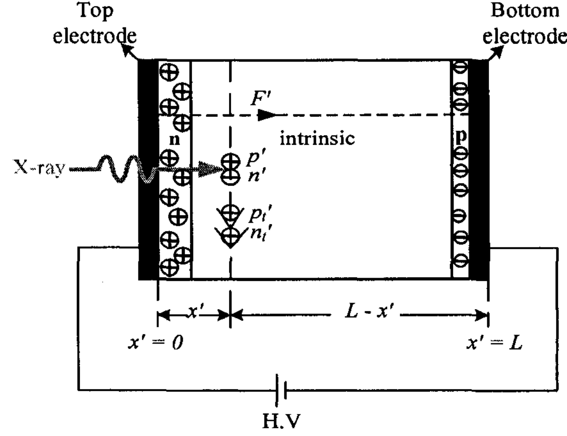

Figure 3.2 Schematic diagram of present model illustrating a three-layer photoconductor sandwiched between two large area parallel plate electrodes used in the model. An electron and a hole are generated at x' and are drifting under the influence of the electric field F'. Holes and electrons are trapped in n and p layers respectively right after applying H.V.

(i) The continuity equations for electrons and holes when positive bias is applied through the sample are,

$$\frac{\partial n'}{\partial t'} = \mu_e \frac{\partial (n'F')}{\partial x'} - \frac{n'}{\tau_e'} - c_e n' p_t' + g(x',t') e^{-\alpha x'}, \tag{3.7}$$

$$\frac{\partial p'}{\partial t'} = -\mu_h \frac{\partial (p'F')}{\partial x'} - \frac{p'}{\tau_h'} - C_h p' n_t' + g(x',t') e^{-\alpha x'}, \tag{3.8}$$

where $F'(x', t')$ is the electric field in the photoconductor, $g(x', t')$ is the electron hole pair (EHP) generation rate, α is the linear attenuation coefficient of the photoconductor, C_e is the capture coefficient between free electrons and trapped holes, and C_h is the capture coefficient between free holes and trapped electrons. For an a-Se photoconductor, a recombination-type capture process follows the *Langevin recombination* mechanism [58-59] and thus $C_h = e\mu_h/\varepsilon$ and $C_e = e\mu_e/\varepsilon$. It is worth to say that the bulk recombination is ignored due to the small signal radiation.

(ii) The trapping rate equations for deep trapping are as follows;

$$\frac{\partial p_t'}{\partial t'} = \frac{p'}{\tau_h'} - C_e n' p_t', \tag{3.9}$$

$$\frac{\partial n_t'}{\partial t'} = \frac{n'}{\tau_e'} - C_h p' n_t'. \tag{3.10}$$

(iii) The poisson equation is,

$$\frac{\partial F'}{\partial x'} = \frac{e}{\varepsilon}(p' + p_t' - n' - n_t'). \tag{3.11}$$

Considering X-ray induced meta-stable deep trap center generation and trap filling, the trapping times for electrons and holes are, respectively [13],

$$\tau_e' = \frac{\tau'_{0e}}{1 + (N_{Xe} - n_t)/N_{0e}}, \tag{3.12}$$

$$\tau_h' = \frac{\tau'_{0h}}{1 + (N_{Xh} - p_t)/N_{0h}}, \tag{3.13}$$

where $N_{Xe(h)}$ is the concentration of X-ray induced deep trap centers, N_0 is the concentration of initial deep trap centers, and τ_0 is the initial carrier trapping time. The concentration of X-ray induced deep trap centers depend on the photoconductor material, the irradiation energy and the amount of exposure. The X-ray induced deep trap center generation kinetics is taken to be a first rate equation such that [39]

$$N_{Xe}(X) = N_{se}[1 - \exp(-\frac{X}{D})], \tag{3.14}$$

$$N_{Xh}(X) = N_{sh}[1 - \exp(-\frac{X}{D})], \tag{3.15}$$

where N_s is the saturation value of the X-ray induced deep trap centers, D is an irradiation energy dependent constant, and X is the amount of accumulated exposure. The value of D is usually large compared to typical exposures in medical X-ray imaging and thus the

meta-stable deep trap center generation is almost proportional to the accumulated X-ray exposure.

The effects of charge transport properties ($\mu\tau'$) and attenuation coefficient of photoconductor materials on the detector performances depend on L and F_0 through the following normalized parameters; the normalized attenuation depth (attenuation depth/thickness) $\Delta = 1/(\alpha L)$, the normalized electron schubweg (electron schubweg per unit thickness) $\tau_e = \mu_e \tau'_e F_0/L$ and, the normalized hole schubweg (hole schubweg per unit thickness) $\tau_h = \mu_h \tau'_h F_0/L$. The schubweg ($\mu\tau' F$) is the distance a carrier drifts before it is deeply trapped and unavailable for conduction. Equivalently, τ_e and τ_h are the normalized carrier lifetimes (carrier lifetimes per unit transit time) for electrons and holes, respectively. For simplicity, we use the normalized distance coordinate x, where $x = x'/L$. The time coordinate is normalized with respect to the transit time of electrons t_e ($t_e = L/\mu_e F_0$, t_e is the longest transit time). Therefore, the normalized time coordinate $t = t'/t_e$. The normalized electric field, $F = F'/F_0$. Charge carrier concentrations are normalized with respect to the total photogenerated charge carriers per unit area, Q_0 (electrons / m^2) in the photoconductor as if the total charge carriers are uniformly distributed over the sample volume.

Let g_0 be the EHP generation rate for a uniform electric field of F_0. Then, the total collectable EHPs generated in the photoconductor layer per m^2 are given by [60],

$$Q_0 = p_0 L = \int_0^T \int_0^L g_0 e^{-\alpha x'} dx' dt' = \frac{5.45 \times 10^{17} X \eta}{(\alpha_{\text{air}} / \rho_{\text{air}}) W_0} \left(\frac{E_{\text{ab}}}{E} \right), \tag{3.16}$$

where T is the exposure time, $\eta = 1 - \exp(-1/\Delta)$ is the quantum efficiency of the detector, E_{ab} is the average absorbed energy per X-ray photon of energy E, X is the exposure (X is

in Roentgens), W_0 is the EHP creation energy (W_0 is in eV) of the photoconductor for electric field of F_0 and incident photon energy of E, α_{air} and ρ_{air} are the energy absorption coefficient and the density of air respectively (α_{air}/ρ_{air} is in cm^2 g^{-1}).

The equations (3.7) through (3.11) can now be recast into the dimensionless forms:

$$\frac{\partial n}{\partial t} = \frac{\partial (nF)}{\partial x} - \frac{n}{\tau_e} - fc_0 np_t + Ke^{-\frac{x}{\Delta}}, \quad (3.17)$$

$$\frac{\partial p}{\partial t} = -r_\mu \frac{\partial (pF)}{\partial x} - r_\mu \frac{p}{\tau_h} - fc_0 r_\mu pn_t + Ke^{-\frac{x}{\Delta}}, \quad (3.18)$$

$$\frac{\partial p_t}{\partial t} = r_\mu \frac{p}{\tau_h} - fc_0 np_t, \quad (3.19)$$

$$\frac{\partial n_t}{\partial t} = \frac{n}{\tau_e} - fc_0 r_\mu pn_t, \quad (3.20)$$

and

$$\frac{\partial F}{\partial x} = c_0[p + p_t - n - n_t], \quad (3.21)$$

where $r_\mu = \mu_h/\mu_e$, $c_0 = eQ_0/\varepsilon F_0$, $n = n'/p_0$, $p = p'/p_0$, $n_t = n'_t/p_0$, $p_t = p'_t/p_0$, and $K(x,t) = \{t_e W_0\}/\{T\eta\Delta\ W(x,t)\}$. The ratio $W_0/W(x,t) = g(x,t)/g_0$. $W(x,t)$ is the electron hole pair creation energy at the instantaneous electric field $F(x,t)$.

During the dark-time, the equations (3.21) through (3.25) are still valid except the carrier generation term, Kexp($-x/\Delta$), in equations (3.17) and (3.18) must be replaced by the carrier injection rates g_{de} and g_{dh}, respectively. Figure 3.3 shows the sample during dark-time.

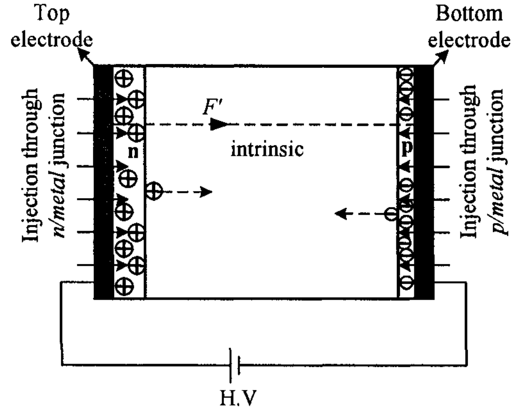

Figure 3.3 The schematic of positively biased sample showing the sample status and generation within the dark-time. The generation is due to injection.

It can be assumed that the carrier trapping due to the dark current, over a long time, is effectively uniform in the blocking layers. The trapped carriers in the blocking layers reduce the electric field at the metal/a-Se interfaces, which reduces the subsequent carrier injections and thus reduces the dark current. Assuming blocking contacts, the injected current densities in low mobility (mobility, $\mu < 1$ cm^2/V-s) semiconductor due to hole and electron injections in *n-i-p* structure are given by, [61]

$$J_h(t) = e\mu_h N_V F_1(t)\exp\left\{-\frac{\phi_h - \gamma\beta_s\sqrt{F_1(t)}}{kT}\right\}, \tag{3.22}$$

$$J_e(t) = e\mu_e N_C F_2(t)\exp\left\{-\frac{\phi_e - \gamma\beta_s\sqrt{F_2(t)}}{kT}\right\}. \tag{3.23}$$

Therefore, the expressions of g_{de} and g_{dh} are given by, [61]

$$g_{dh}(1,t) = \frac{N_V t_e}{p_0 T}\exp\left\{-\frac{\phi_h - \gamma\beta_s\sqrt{F_1(t)}}{V_t}\right\}, \tag{3.24}$$

$$g_{de}(0,t) = \frac{N_C t_e}{p_0 T}\exp\left\{-\frac{\phi_e - \gamma\beta_s\sqrt{F_2(t)}}{V_t}\right\}, \tag{3.25}$$

where $F_1(t)$ is the instantaneous electric field at the metal/n layer interface, $F_2(t)$ is the instantaneous at the metal/p-layer interface, $\beta_s = \sqrt{\frac{e^3}{4\pi\varepsilon}}$ is the Schottky coefficient, ε $(=\varepsilon_0 \varepsilon_r)$ is the permittivity of the photoconductor, V_t is the thermal voltage, $N_{V(C)}$ is the effective density of states in the valence (conduction) band, φ is the effective barrier height for injecting carriers from metal into the blocking layers considering the effect of surface states. Here, γ is a fitting parameter and close to unity. The subscripts h and e stands for holes and electrons respectively.

Equations (3.17) through (3.21) are nonlinearly coupled partial differential equations. These nondimensionalized coupled equations are simultaneously solved by the finite difference method. After applying high voltage, it is assumed that there is an enough interval time for the dark current to reach a stable state before any exposure. With this assumption, the necessary initial conditions are,

$$n(x,0) = 0, \quad p(x,0) = 0, \quad p_t(x,0)_i = n_t(x,0)_i = 0,$$
$$p_t(x,0)_n = p_{t0}, \quad n_t(x,0)_p = n_{t0} \tag{3.26}$$

where indices of i, n , or p represent the intrinsic, n, and p layers. The initial $F(x, 0)$ and the instantaneous electric field $F(x,t)$ can be determined by solving the equation (3.21) with a boundary condition *i.e.*,

$$\int_0^1 F(x,t)dx = 1 \ . \tag{3.27}$$

After EHP generation due to an X-ray exposure, one type of carrier drifts towards the radiation-receiving electrode (top electrode) and the other type of carrier drifts towards the other electrode (bottom electrode). For positive bias, electrons move towards the radiation-receiving electrode and holes move towards the bottom electrode. Therefore,

right after (or shortly after) X-ray exposure, the free hole concentration at $x = 0$ and the free electron concentration at $x = 1$ are zero since the carriers would have started drift. The total normalized current density due to X-ray generated carriers is given by [62-63],

$$j(t) = \int_0^1 F(x,t)\left[n(x,t) + r_\mu p(x,t)\right]dx \,. \tag{3.28}$$

The integration of current over time period of interest is the normalized collected charge or charge collection efficiency. The product of the normalized collected charge and the quantum efficiency represents the normalized X-ray sensitivity.

A considerable amount of hole detrapping is expected during an experimental study of ghosting. The detrapped carrier can be trapped again in an arbitrary position and can later be detrapped. For simplicity, the resultant amount of detrapped carriers can be estimated by assigning an average detrapping time and neglecting further trapping. There is a time gap of t_{off} of few minutes (typically 1 to 5 minutes) between two successive X-ray exposures. The hole detrapping probability within time t_{off} for a carrier with a detrapping time τ_{rh} is $[1-\exp(-t_{off}/\tau_{rh})]$.

Figure 3.4 shows the schematic of positively biased sample showing the virtual process of hole detrapping and re-trapping during the dark-time.

The current density due to detrapping of holes at positive and negative bias is given, respectively, [64],

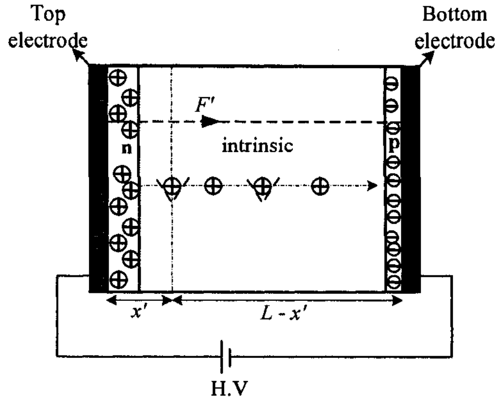

Figure 3.4 The schematic of positively biased sample showing the virtual process of hole detrapping and re-trapping during the dark-time.

$$j_r(t) = \int_0^1 \frac{p_t(x,t)\exp(-\frac{t}{\tau_{rh}})}{\tau_{rh}}(1-x)dx, \tag{3.29}$$

$$j_r(t) = \int_0^1 \frac{p_t(x,t)\exp(-\frac{t}{\tau_{rh}})}{\tau_{rh}}(x)dx. \tag{3.30}$$

The amount of collected charges due to hole detrapping is calculated by integrating the current over the time gap (dark-time). The collected charge due to the detrapped holes will be added to the collected charges due to the exposure and dark current.

3.5 Theoretical Ghosting Recovery Model for Multilayer a-Se Detectors

The reduced sensitivity of the sample is eventually recovered with time by resting the sample. During resting period the trapped carriers and the amount of meta-stable trap centers are released exponentially with time. Therefore, the time-dependent concentrations of trapped carriers and meta-stable trap centers are given by,

$$p_t(x,t+\Delta t) = p_t(x,t)\exp(-\frac{\Delta t}{\tau_{rh}}), \tag{3.31}$$

$$n_t(x,t+\Delta t) = n_t(x,t)\exp(-\frac{\Delta t}{\tau_{re}}), \tag{3.32}$$

$$N_{Xh}(X,t+\Delta t) = N_{sh}(1-e^{-\frac{X}{D}})\exp(\frac{-\Delta t}{\tau_{rN}}), \tag{3.33}$$

and

$$N_{Xe}(X,t+\Delta t) = N_{se}(1-e^{-\frac{X}{D}})\exp(\frac{-\Delta t}{\tau_{rN}}), \tag{3.34}$$

where Δt is the infinitesimally small time step, $\tau_{rh(e)}$ is the release time of holes (electrons), and τ_{rN} is the characteristic decay time for the meta-stable trap centers.

The experimental sequence of different pulses is shown in Figure 3.5 Initially and in the first step, test pulses are used to measure the sensitivity. The dose of each test pulse is much less than that of ghosting pulse. Therefore, the sensitivity reduction of the sample is negligible when the test pulses are illuminated. In the second step, the sample is exposed by the ghost pulse so that the desirable amount of ghost can be achieved. In the third step, the recovery process begins in which the test pulses are again used to measure the sensitivity.

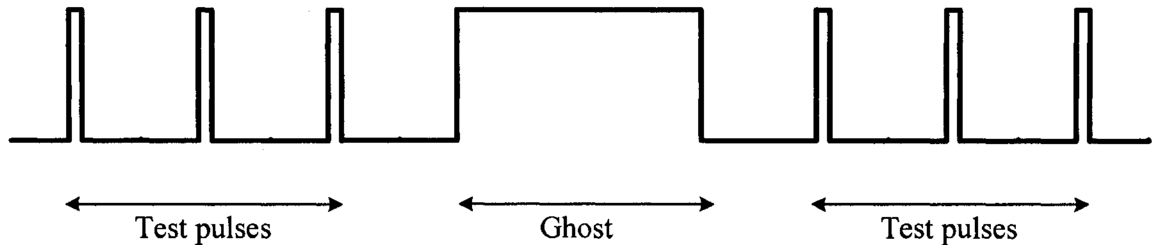

Figure 3.5 Three different steps of ghosting recovery simulation, (i) reading the initial sensitivity by radiating test pulses, (ii) radiating ghost pulse, (iii) recovery process, radiating the test pulses.

There is a dark-time of around 2-5 minutes between each two successive test pulses. It is necessary to say that the approach used to model and simulate the ghosting recovery process is the same as ghosting model described in section 3.3.

Chapter 4

Results and Discussions

In this chapter the measurement results which have been obtained through experimental studies of ghosting and its recovery along with their simulation results are presented. The objectives of this chapter are,

(i) To report the effects of the blocking layers (*n, p*) on relative sensitivity of the detector and electric field profile (charge distribution) across the sample,

(ii) To study the ghosting in a multilayer a-Se based detector while charge injection (dark current) through *metal / n(p)* is taken into account,

(iii) To study the dark current change versus accumulated exposure and time,

and

(iv) To present the experimental study and measurement results of ghosting and its natural recovery process. The results of theoretical study are compared with related experimental data obtained through experiments. In this section the effects of different factors contributing in natural ghosting recovery are studied.

4.1 Sensitivity Reduction and Ghosting

The instantaneous electric field, free and trapped carrier distributions are obtained by numerically solving the equations (3.17) through (3.21) with appropriate initial and the boundary conditions during both exposure and dark-times. The relative X-ray sensitivity is calculated as a function of accumulated X-ray exposure or dose. The relative X-ray sensitivity is obtained by normalizing the sensitivity by the expected sensitivity before

any X-ray exposure. The amount of EHP generation from a fixed exposure is calculated using equation (3.16). The electron-hole-pair creation energy $W_{\pm}$ in a-Se has a strong dependence on the electric field and weak dependence on the X-ray photon energy [28-29]. The quantity $W_{\pm}$ decreases with increasing electric field and photon energy. The values of $W_{\pm}$ were taken from the work of Blevis, Hunt, and Rowlands [28].

The numerical model is fitted to the experimental data. For a positively biased sample the applied electric field, F_0 = 3 V/μm and L = 498 μm, and therefore, Δ = 1.56. The thicknesses of the n and p layers are assumed to be 20 μm and 5 μm as described in [5]. The hole detrapping time is assumed as $\tau_{dh} \approx 10$ minutes in all three layers (n-i-p) and $N_0 \approx 5 \times 10^{18}$ m^{-3} for both holes and electrons in the intrinsic layer. The quantity N_0 in the n and p layers is assumed to be 10^{21} m^{-3} in the present calculations. Figure 4.1 (a) shows the relative sensitivity of a n-i-p detector as a function of accumulated X-ray exposures. The closed circles in Figure 4.1 (a) represent the experimental data. The average photon energy E_{av} is 55 keV for an 80 kVp applied X-ray spectrum with 23.5 mm Al filtration. The mobility-lifetimes of carriers in intrinsic layer are $(\mu_h \tau'_{0h})_i \approx 3.5 \times 10^{-6}$ cm^2/V and $(\mu_e \tau'_{0e})_i \approx 2.2 \times 10^{-6}$ cm^2/V (experimentally measured values). The integration time for the signal collection is 1 second within the 2-min dark-time. The numerical results considering effective recombination coefficient (f = 0.25) in all three layers in the present model agree well with experimental data. The fitted values of N_{se} (=N_{sh}) and D are 1.5 $\times 10^{19}$ m^{-3} and 2 R, respectively. The recombination between trapped and the oppositely charged drifting carriers, and X-ray induced new deep trap centers are mainly responsible for ghosting in multilayer a-Se-based X-ray detectors the same as monolayer a-Se based detectors [13].

Figure 4.1 (b) shows the field distributions across the photoconductor under positive bias for different accumulated X-ray exposures. The electric field at the radiation-receiving electrode increases with increasing cumulative exposure. The electric field distributions reach a steady value after a large accumulated exposure. Since the X-ray absorption profile is exponential across the photoconductor, it is expected that the total EHP generation is somewhat greater under positive bias because most of the X-ray photons are absorbed in the high field region.

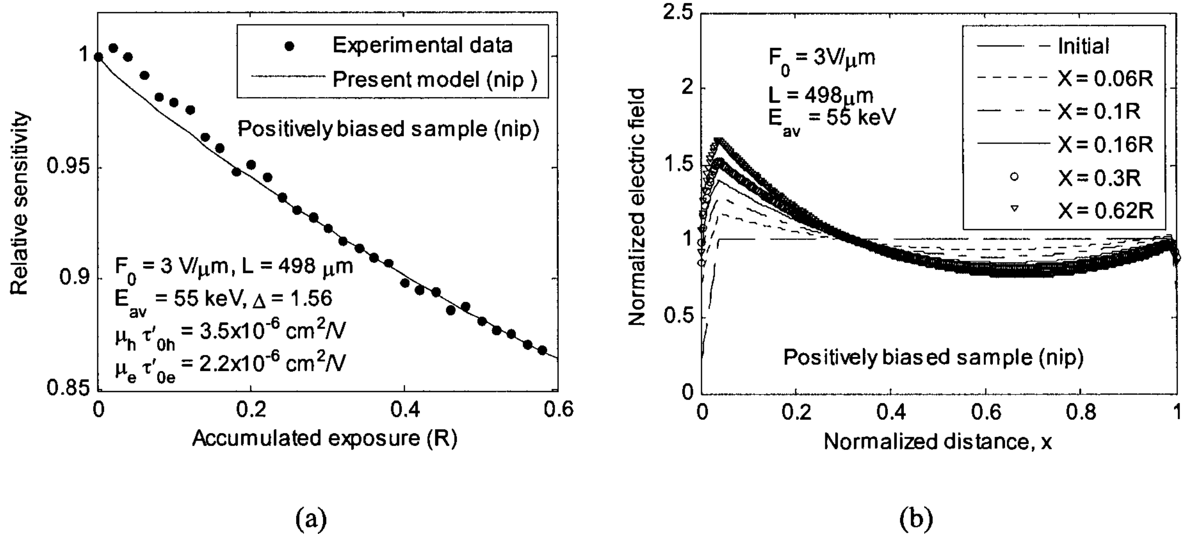

(a) (b)

Figure 4.1 (a) Relative X-ray sensitivity vs. accumulated X-ray exposure for a positively biased *n-i-p* a-Se detector. The closed circles represent experimental data and the solid line represents the theoretical fit to the experimental data. (b) The electric distributions across the photoconductor for different cumulative X-ray exposures [57].

Figure 4.2 shows the effect of blocking layers on electric field across the positively biased sample. As is obvious, adding *n* and *p* layers decreases the electric field at the two ends and particularly at the top end (in positively biased sample) where the most amount of generation is expected.

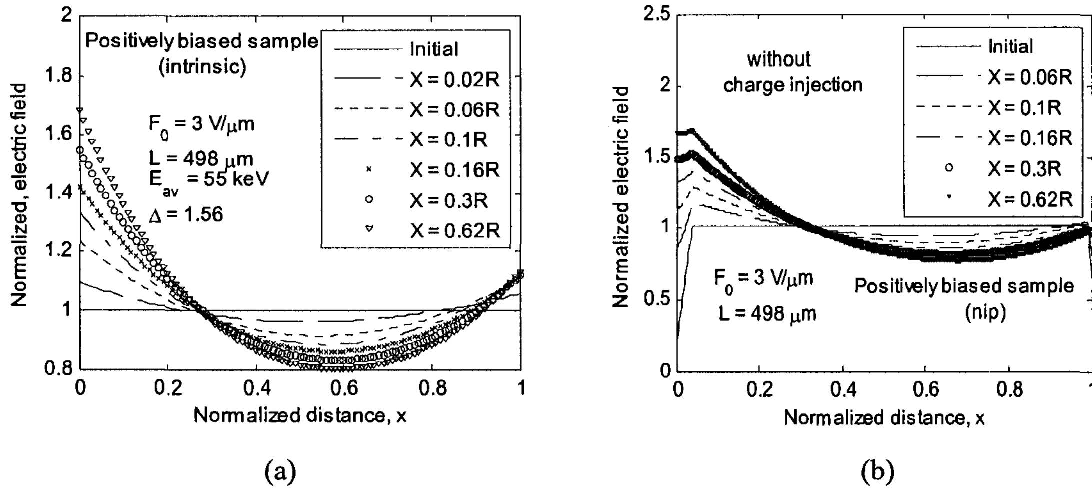

(a) (b)

Figure 4.2 (a) Electric field profile for a positively biased intrinsic sample considering an effective recombination coefficient (f = 0.25), including holes detrapping during 2-min dark-time, Collection of detrapped holes in 1 sec, (b) the electric field of the *n-i-p* sample, including hole detrapping, the same conditions as Figure 4.2 (a).

As mentioned above, the electric field in the blocking layers is lower than that of a monolayer (intrinsic layer) sample. Therefore, the X-ray sensitivity of *n-i-p* detector is somewhat lower than that of a monolayer detector as shown in Figure 4.3. The effect of dark current on absolute sensitivity is also shown in Figure 4.3. A visual inspection of Figure 4.3 shows that the contribution of the dark current on absolute sensitivity is not significant [57].

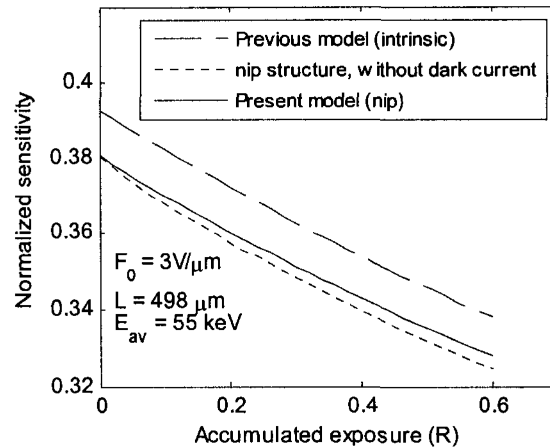

Figure 4.3 A comparison of the normalized sensitivity in a monolayer based detector (previous model) [13] shown with dashed line, a *n-i-p* based detector without injection shown with dotted line, and present model shown with solid line (positively biased, present model) [57].

The normalized charge distributions across the photoconductor are shown in Figure 4.4. As illustrated the concentration of holes and electrons are significantly large in *n* and *p* layers respectively. The concentration of holes and electrons in *n* and *p* layers respectively are determined by EHP generation due to X-ray radiation, charge injections and charge detrapping.

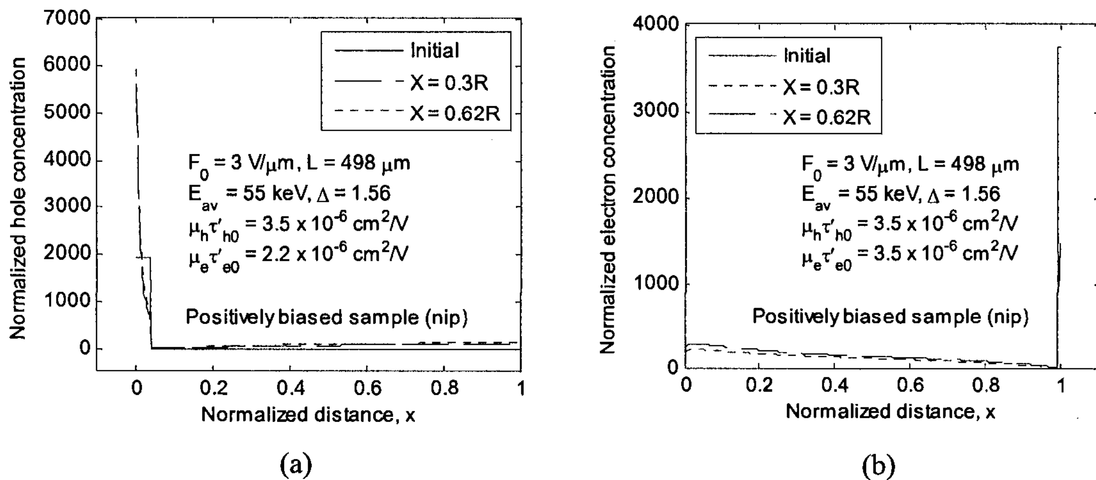

(a) (b)

Figure 4.4 (a) The normalized hole concentration, and (b) the normalized electron concentration across the positively biased sample

Figure 4.5 (a) shows the relative X-ray sensitivity as a function of accumulated exposure for a negatively biased *p-i-n* a-Se detector. The electric field F_0 = 6 V/μm and L = 1000 μm, and therefore, Δ = 0.78. The mobility–lifetimes of carriers are measured as $(\mu_h \tau'_{0h})_i \approx 5.7 \times 10^{-6}$ cm^2/V and $(\mu_e \tau'_{0e})_i \approx 5.2 \times 10^{-6}$ cm^2/V. The hole detrapping time τ_{dh} = 10 minutes in all three layers (*p-i-n*), and $N_0 = 3 \times 10^{18}$ m^{-3} for both holes and electrons in the intrinsic layer. All other parameters are the same as in Figure 4.1. The numerical results considering effective recombination coefficient (f = 0.3) in all three layers in the present model agree well with experimental data. Fitted values of N_{se} (=N_{sh}) and D are 1.6×10^{19} m^{-3} and 1.5 R, respectively. Figure 4.5 (b) shows the field distributions across the photoconductor for different accumulated X-ray exposures. The electric field at the positive electrode (bottom electrode) increases with increasing cumulative exposure.

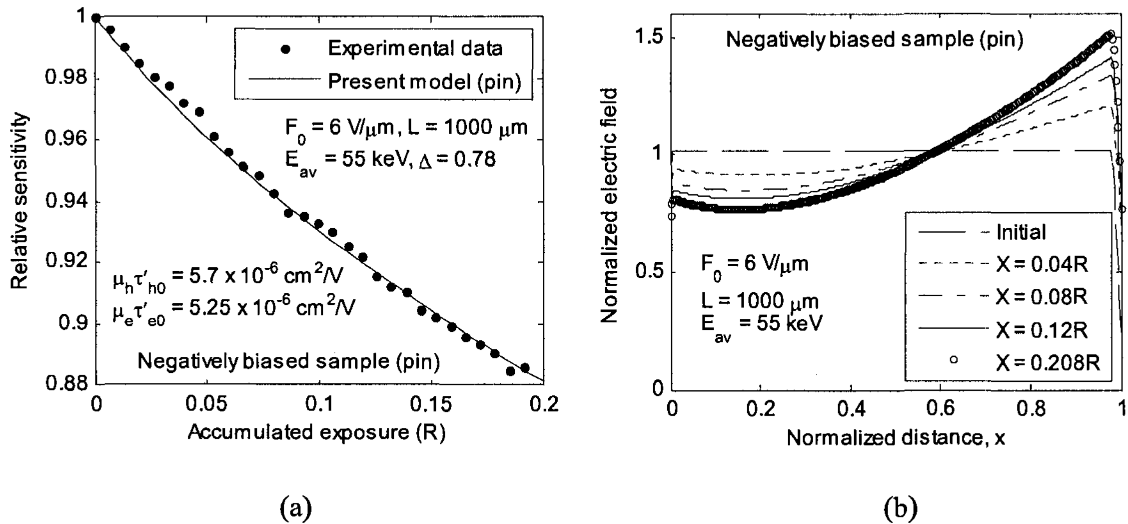

(a) (b)

Figure 4.5 (a) Relative X-ray sensitivity versus cumulative X-ray exposure for a negatively biased *p-i-n* a-Se detector. The closed circles represent experimental data and the solid line represents the theoretical fit to the experimental data [57]. (b) The electric distributions across the photoconductor for different cumulative X-ray exposures [57].

Figure 4.6 shows the effect of blocking layer on electric field across the negatively biased sample. As is obvious, adding *n* and *p* layers decreases the electric field at the two ends but particularly at the bottom and as opposed to that in positively biased sample.

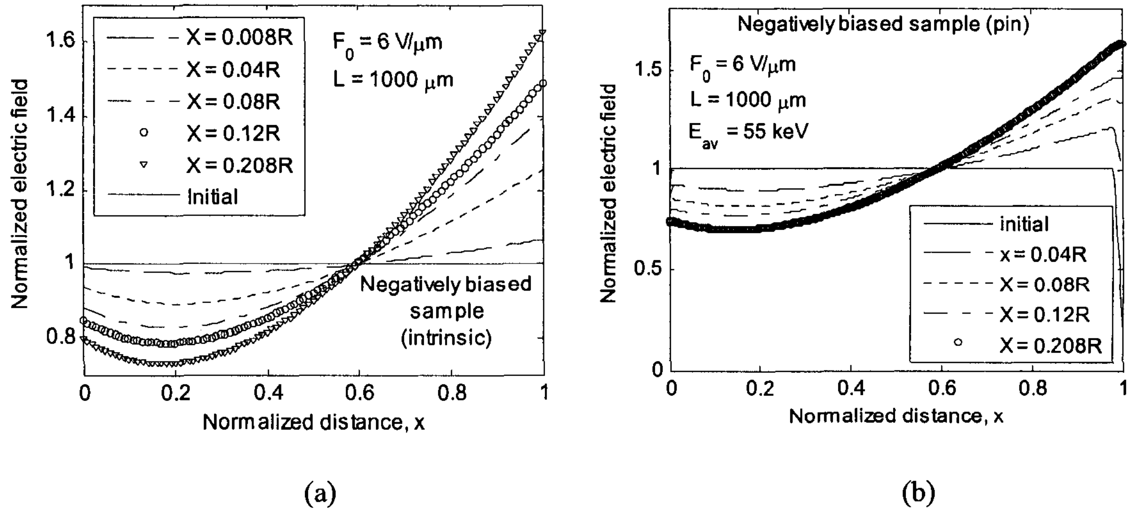

(a) (b)

Figure 4.6 (a) Electric field profile for a negatively biased intrinsic sample considering an effective recombination coefficient (f = 0.3), including holes detrapping during 2-min dark-time, Collection of detrapped holes in 1 sec (b) the electric field of the *p-i-n* sample, including hole detrapping, without charge injection.

It is evident from Figures 4.1 (b) and 4.5 (b) that the reduction in electric field at the radiation receiving electrode in negatively biased sample is much less than that in positively biased sample which causes less reduction in sensitivity due to the blocking layer in negatively biased sample. Therefore, by including charge injection into the model the normalized sensitivity of the present model will be somewhat higher than the previous model.

Figure 4.7 shows the comparison of normalized sensitivity among three different scenarios including previous model (intrinsic sample), *p-i-n* based sample while charge injection is ignored, and the complete model including charge injection.

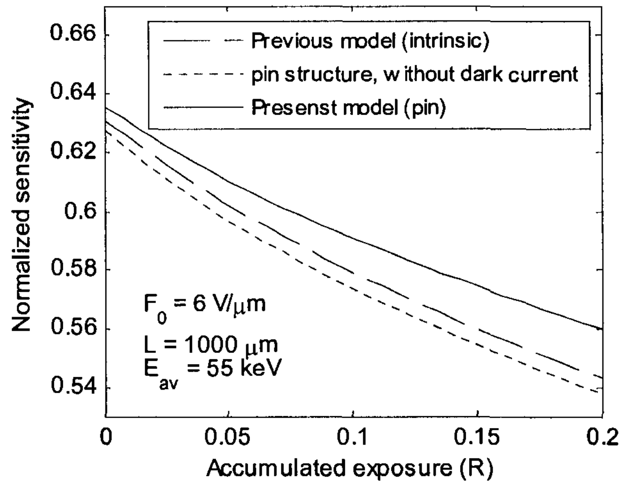

Figure 4.7 A comparison of the normalized sensitivity in a monolayer based detector (previous model) [13], and a *p-i-n* based detector (negatively biased, present model), the effect of dark current is also shown.

For the negatively biased sample, or *p-i-n* based structure, the normalized charge distributions across the photoconductor are shown in Figure 4.8. The same scenario mentioned and illustrated in Figure 4.4 for positively biased sample is true for negatively biased sample, except that the *p* and *n* layers are in the top and bottom electrodes. As illustrated the concentration of electrons and holes are significantly large in *p* and *n* layers respectively. The concentration of holes and electrons in *n* and *p* layers respectively are determined by EHP generation due to X-ray radiation, charge injections and charge detrapping.

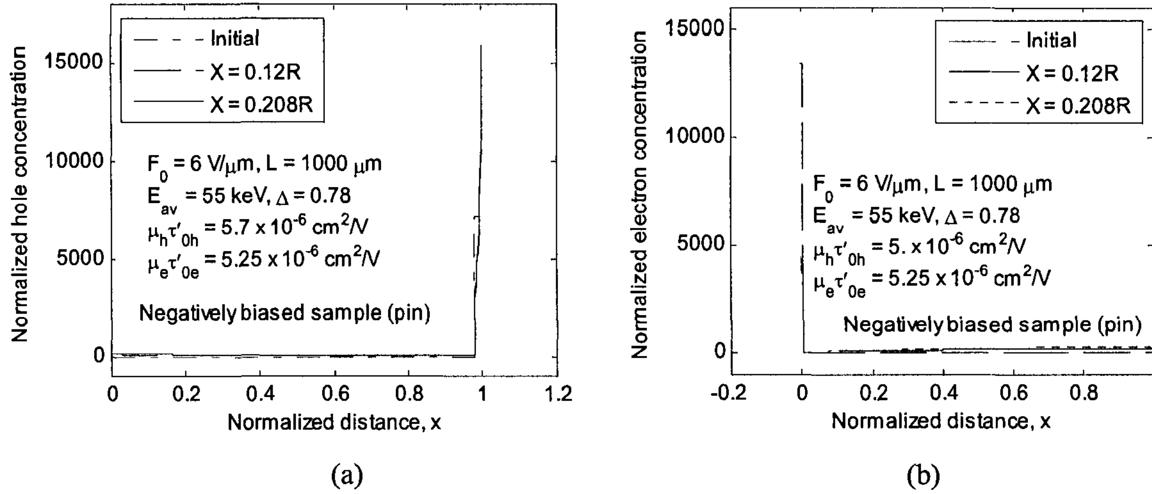

Figure 4.8 (a) The normalized hole concentration, and (b) the normalized electron concentration across the negatively biased sample determined by the three most important phenomena i) EHP generation due to X-ray radiation, ii) charge injections, iii) hole detrapping.

It is also evident from Figure 4.1 (b) and 4.5 (b) that the electric fields at both contacts increase with accumulated X-ray exposure. The dark current increases with increasing contact electric fields as is obvious from equations (3.22), and (3.23). Therefore, it is instructive to calculate the change in dark current during the experimental study of ghosting. Figure 4.9 (a) and (b) show the relative dark current density as a function of time.

It is worth to say that the initial amount of dark current is calculated based upon the assumption that there is enough interval time between applying the high voltage and the first exposure so the initial dark current density for both positively and negatively biased detectors is the steady state dark current after applying the bias voltage but before any exposure. The initial amount of dark current density is ~ 7 pA/cm^2 and ~ 25 pA/cm^2 for positively and negatively biased respectively.

The concentration of the trapped holes and electrons in *n* and *p* layers respectively, determine the electric field at the two very ends of the sample. These concentrations are calculated based on the recent dark current model for stabilized a-Se [61]. During ghosting measurement, the dark current density is calculated at the end of the dark-time and right before the next exposure. There are 31 radiation pulses for positively biased sample, and 26 pulses for negatively biased sample.

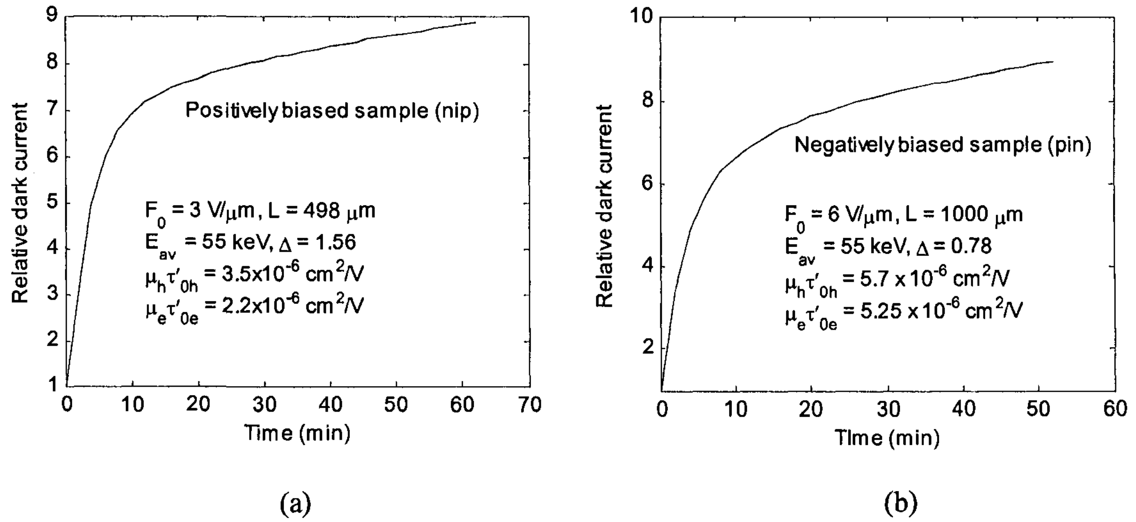

(a) (b)

Figure 4.9 (a) Relative dark current density vs. time for positively biased sample, (*n-i-p* based sample), with the conditions set for Figure 4.1 (b) relative dark current vs. time for negatively biased sample, (*p-i-n* based sample), with the conditions set for Figure 4.5.

As illustrated in both Figures 4.9 (a) and (b), the increase of dark current density is almost an order of magnitude, which has also been observed previously. In both biases, the relative dark current increases quickly during first few exposures and, after that, the rate of increase decreases with time.

The amount of ghosting strongly depends on the applied electric field. Figure 4.10 shows the relative sensitivity as a function of cumulated X-ray exposure and normalized electric field across the positively biased a-Se detector for the initial electric field F_0 = 6 V/μm.

The circles represent experimental data and the solid line represents numerical results. The theoretical result agrees well with the experimental data. All other parameters in Figure 4.10 are the same as in solid curve in Figure 4.1. The recombination coefficient f varies between 0.25 and 0.3. This change in the recombination coefficient is not fully known. In Figure 4.11 the same scenario as mentioned above is shown for negatively biased sample. All other parameters in Figure 4.11 are the same as in solid curve in Figure 4.5.

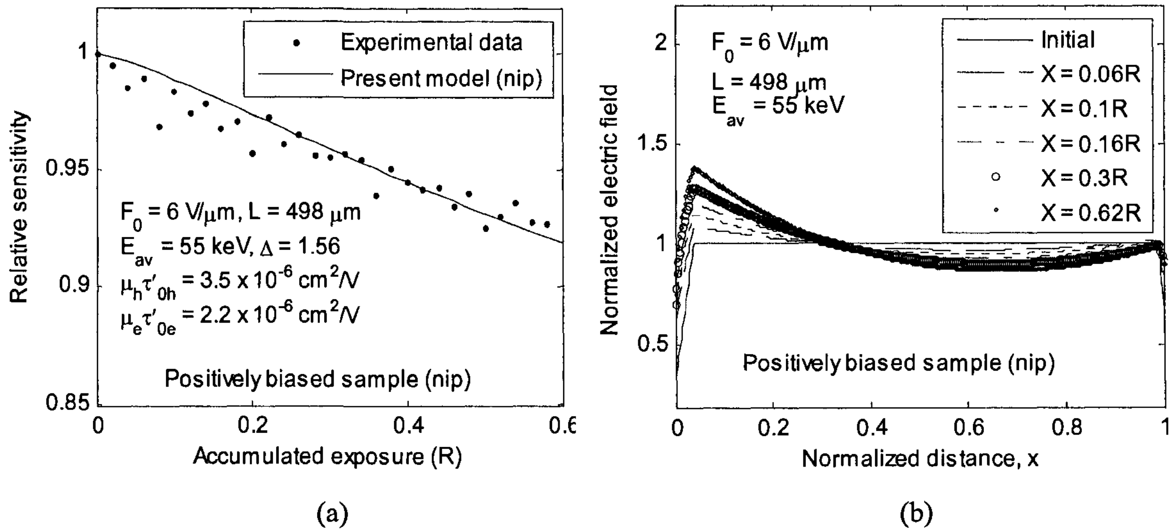

(a) (b)

Figure 4.10 (a) The relative sensitivity of a *n-i-p* based sample including charge injection and hole detrapping, collection of injected charges and detrapped holes is performed within 1 second during 2-min dark-time. (b) The electric field profile for the same sample.

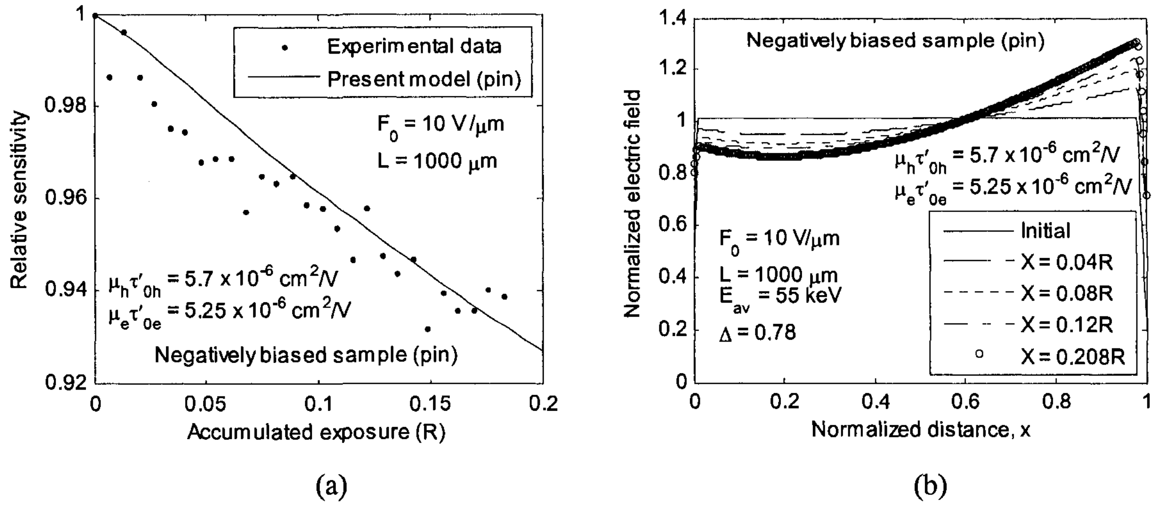

(a) (b)

Figure 4.11 (a) The relative sensitivity of a *p-i-n* based sample including charge injection and hole detrapping, collection of injected charges and detrapped holes is performed within 1 second during 2-min dark-time. (b) The electric field profile for the same sample.

Figure 4.12 (a) and (b) show the relative dark current density as a function of time for the electric of F_0 = 6 V/μm and F_0 = 10 V/μm. A visual inspection of Figure 4.12 shows that the behaviour of the dark current remains the same as Figure 4.9 except the level of increase of the dark current seems to be lower. This difference is because of the different levels of changing in the electric fields at the two ends for both the cases that can be compared from Figures 4.10 (b) and 4.1 (b) for positively biased sample, and Figure 4.11 (b) and 4.5(b) for negatively biased sample. The initial dark current is ~ 25 pA/cm^2 and ~ 40 pA/cm^2 for positively and negatively biased sample respectively.

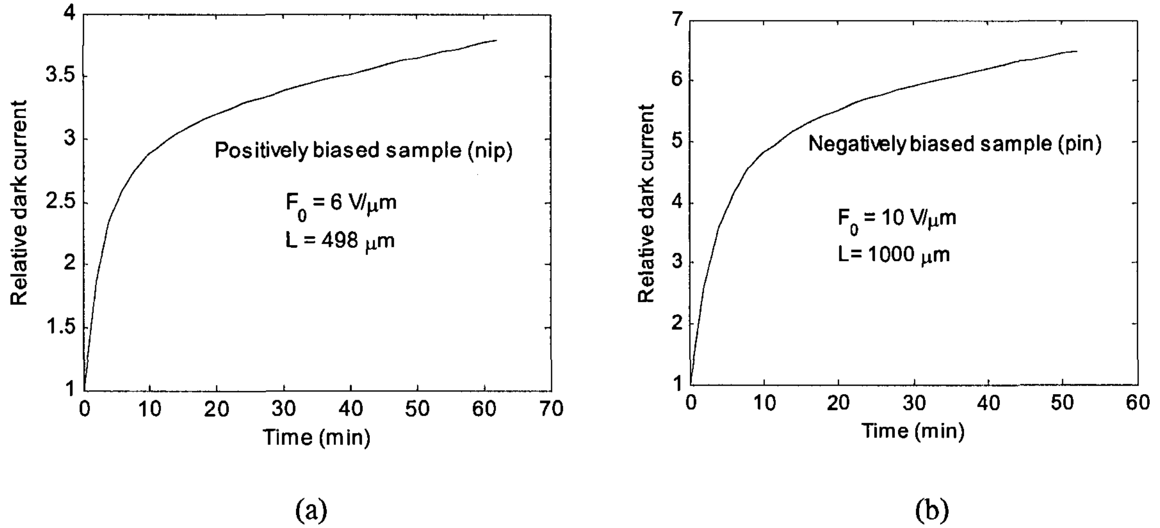

(a) (b)

Figure 4.12 (a) Relatibe dark current density vs. time for positively biased sample, (*n-i-p* based sample), with the conditions set for Figure 4.10 (b) relative dark current vs. time for negatively biased sample, (*p-i-n* based sample), with the conditions set for Figure 4.11.

Figures 4.13 (a) and (b) show the relative sensitivity of a positively and negatively biased a-Se detector respectively as a function of cumulative X-ray exposure for different applied electric fields. The exposure dose is 0.08 R for each pulse. There are 31 pulses for positively biased sample and 26 pulses for negatively biased sample. The deep trap center concentration for both holes and electrons is $N_0 \approx 3 \times 10^{18}$ m^{-3} in the intrinsic layer. The quantity N_0 in the *n* and *p* layers is assumed to be 10^{21} m^{-3}.

The ghosting level increases with decreasing applied electric field because of higher carrier trapping rate at lower applied electric fields.

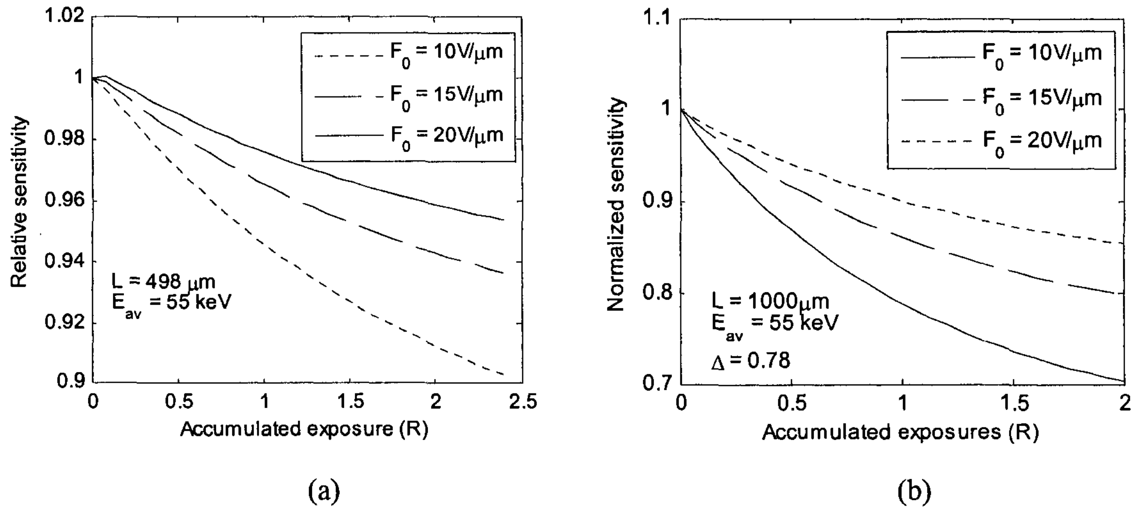

(a) (b)

Figure 4.13 The effect of electric field on the level of ghosting, the more the electric field is the less the amount of ghosting will be, (a) positively biased sample, (b) negatively biased sample in which, $\mu_e \tau'_{0e} \approx 3.5 \times 10^{-6}$ cm^2/V and $\mu_h \tau'_{0h} \approx 9.6 \times 10^{-6}$ cm^2/V.

As shown in Figure 4.13 (a), the relative sensitivity increases a little (0.2%) within the first pulse of radiation for F_0 = 20 V/μm. This phenomenon was observed by B. Zhao and W. Zhao in a specific experiment [65]. Figure 4.14 shows the comparison of relative sensitivities for the same sample while in one case the dark-time is 2 minutes and in the other case is 5 minutes. As illustrated, there is no increase in relative sensitivity when the dark-time is 5 minutes. This phenomenon may happen for some other reasons in addition to the main mechanism of recombination. The longer the dark-time is, the less the trapped electrons will be in the sample. This observable fact is happening due to the injected holes which can recombine with the trapped electrons. As such, the electric field will decrease at the entrance side.

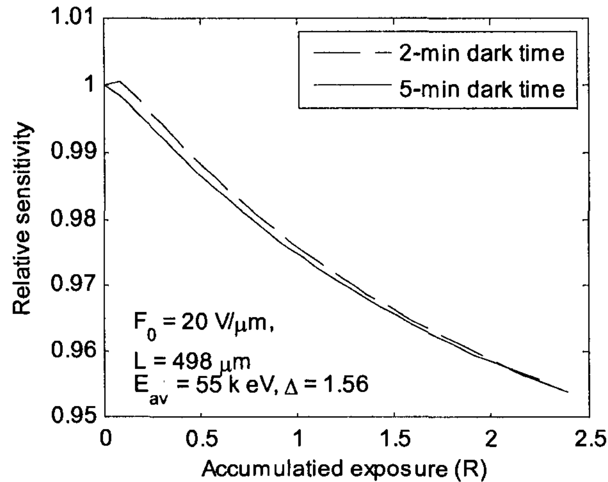

Figure 4.14 The comparison of relative sensitivity between two different dark-times while other conditions are the same. Positively biased sample, (*n-i-p*), all the conditions are the same as Figure 4.13 except electric field and dark-time.

4.2 Ghosting Recovery (Experimental Research)

In this thesis, the change in sensitivity versus accumulated exposure, and time (ghosting and its recovery) has been studied experimentally and theoretically at the same time. Experimental research has been carried out in *Anrad* Corporation, *St-Laurent, Montreal.* A schematic of the setup utilized to accomplish the experiment is shown in Figure 4.15. For this specific experiment (ghosting and recovery), the whole process is automated through a PC. Tool Command Language (*TCL*) is used to select different parameters (*i.e.,* number of test pulses, test pulse dose, dark-time between each two test pulses, ghost dose, number of test pulses in the recovery process,...) .

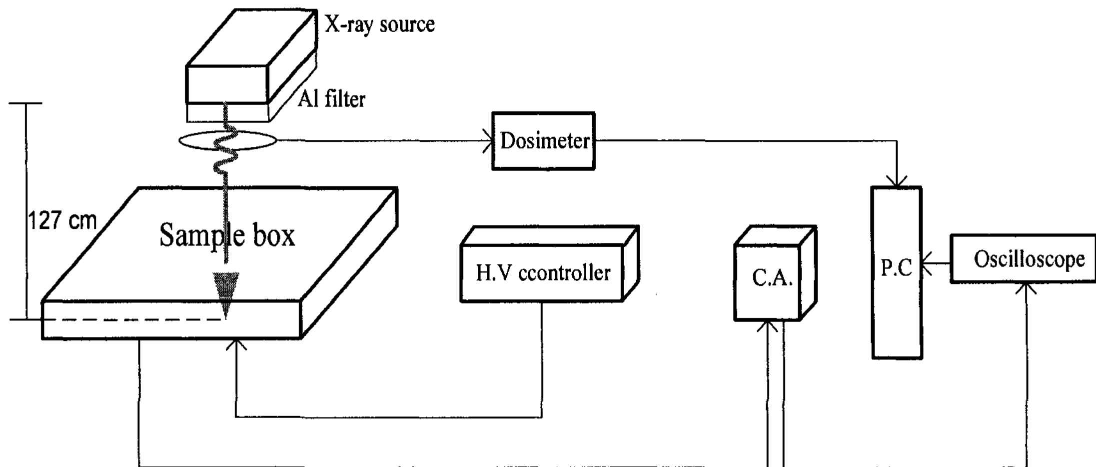

Figure 4.15 A schematic of the setup utilized to carry out the ghosting recovery process. The sample is placed in the sample box. The sensitivity is measured through *PC* using *TCL*.

Each device of the setup is explained below;

X-ray source: X-ray source or X-ray emitter is a box with which different parameters of radiation, *i.e.,* kVp, can be adjusted. This device is temperature limited meaning that if it is over used (large numbers of X-ray pulses are used) an error message will be appeared on the screen of the PC.

Al filter: When medical X-rays are being produced, a thin metallic sheet is placed between the emitter and the target, effectively filtering out the lower energy (soft) X-rays. This filter is often placed close to the window of the X-ray tube. The resultant X-ray is said to be hard. Soft X-rays overlap the range of extreme ultraviolet.

Dosimeter: The dosimeter is used to measure the dosage of radiation. It must be reset before any experiment. The dosimeter is connected to a circular plate placed between the sample and the X-ray source.

Sample box: The sample box includes a plate on which the sample is placed. There are two connections in sample box. One connection is for applying H.V bias, and the other

connection is the output of the sample which is connected to the charge amplifier. The distance between sample and the X-ray source is adjustable.

H.V. controller: This device is used to apply either positive or negative bias to the sample. The device can be used in two modes of operation, remote or local which can be adjusted by a key on the back of the device. To change the type of bias (negative or positive) the device needs to be opened and is not automated.

Charge amplifier (C.A.): The inverting-input of the charge amplifier is connected to the output of the sample. The output of charge amplifier is connected to oscilloscope.

Oscilloscope: On the oscilloscope the wave form can be seen. This wave form is the current produced by collecting the photo-generated electron hole pairs in the sample.

In this thesis experiments have been done so as to study the ghosting and its recovery. Table 4.1 shows important characteristics of the sample used in the experiments

Table 4.1 Characteristics of the *n-i-p* sample used in experimental investigations for ghosting recovery.

Sample: 029 – R745	
Structure	*n-i-p*
Total length (μm)	1000
Dark current density (pA/cm^2)	29
Electron mobility-life time product (cm^2/V)	2.8×10^{-6}
Hole mobility-life time product (cm^2/V)	391×10^{-6} !
Chlorine impurity concentration (ppm)	2

The ghosting recovery measurement is performed on *n-i-p* and *p-i-n* structures following the sequence of Figure 3.6. The average photon energy is 55 keV, for 80 kVp (with 50 mA amplitude of the tube current) applied X-ray spectrum with Al filtration. The test pulse dosage used for these experiments is around 0.5 mR. The pulse width of each radiation is 50 ms.

The reason of adding chlorine to the sample is that it can increase the hole mobility-life time product. In this case, (for *n-i-p* samples) the more number of holes can be collected. The first experiment is performed with the applied electric field of $F_0 = 6$ V/μm. Figure 4.16 shows the result of this experiment. There are 12 test pulses before the ghost pulse is applied. The dark-time between each two test pulses is 2 minutes. It is expected that the sensitivity decreases with applying the ghost pulses. However, as illustrated in this Figure ghost is not observed. The reason of not observing ghost is the relatively high electric field. It is necessary to remind that using this high electric field charge injection is significant.

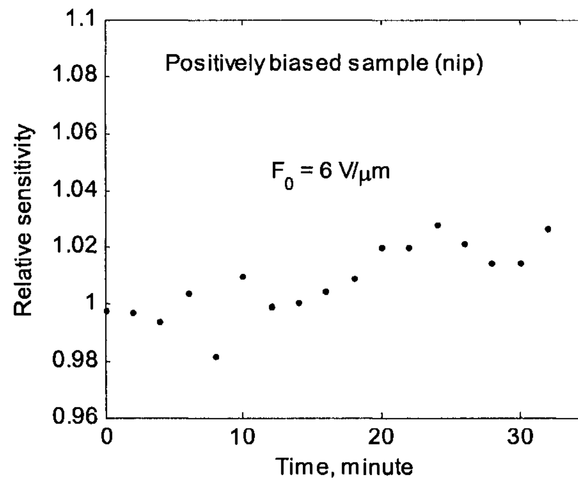

Figure 4.16 Experimental result, $F_0 = 6$ V/μm. Ten test pulses are radiated before the ghost pulse is applied. With applying ghost pulses, sensitivity does not decreases which can be due to the relatively high electric field.

In the next step the electric field is decreased so as to be able to reduce the sensitivity. The ghost pulse is applied after radiating 10 test pulses. This experiment is performed with the electric field of F_0 = 3 V/μm. Applying this voltage, it is possible to get ~ 15% decrease in the relative sensitivity. This result is consistent with the theoretical investigation done to study the effect of electric field on the level of ghosting. The dark-time between each test pulses is 2 minutes.

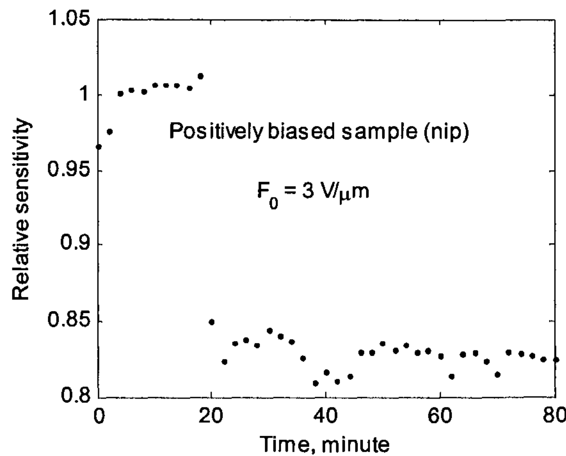

Figure 4.17 Experimental result, F_0 = 3 V/μm. Ten test pulses are radiated before the ghost pulse is applied. With applying ghost pulses relative sensitivity decreases ~ 15%.

As can be seen in Figure 4.17, the ghost is not recovered in the recovery process. The relatively low electric field may prevent the ghost from recovering. Following this experiment, It has been decided to use the electric field of F_0 = 5 V/μm. In this experiment, the Al filter is removed in the course of applying the ghost pulse so as to achieve some level of ghost. Figure 4.18 illustrates the result of such investigation.

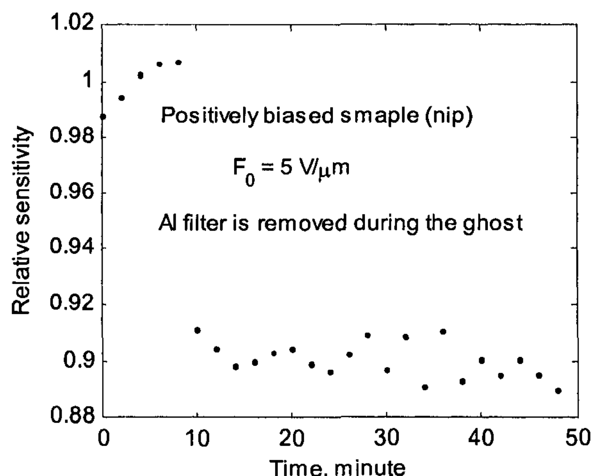

Figure 4.18 Experimental result, $F_0 = 5$ V/μm. Five test pulses are radiated before the ghost pulse is applied. The Al filter is removed during the ghost pulse, (X ~ 15R). (The dark-time between each two test pulses is 2 minutes).

A possible argument about these experiments is the fact that, due to very high hole mobility-life time product of this sample (as indicated in Table 4.1) very small number of holes can be trapped in the sample so basically in this case, there would be few trapped holes which could be released and recover the ghost. It is not necessary to say that in the positively bias sample, there is small number of trapped electrons across the sample. In addition, the electron release time is in the range of several hours, so given the recovery time the effect of electron release may not be significant in this particular experiment.

In addition to the above experiments that have been performed using positively biased sample, the result of other experiments that have been carried out using negatively biased sample will be presented. Table 4.2 shows some important characteristics of the *p-i-n* sample used in these experiments:

Table 4.2 Characteristics of the *p-i-n* sample used in experimental investigations for ghosting recovery.

Sample: 325+328	
Structure	*p-i-n*
Total length (μm)	1088
Dark current density (pA/cm^2)	18
Electron mobility-life time product (cm^2/V)	3×10^{-6}
Hole mobility-life time product (cm^2/V)	35×10^{-6}

As mentioned before, adding chlorine to the sample can basically increase the hole life-time. As in negatively biased sample electrons are collected, there is no need to add chlorine.

The first experiment using negatively biased sample is done by applying the electric field of 5 V/μm. The result is shown in Figure 4.19.

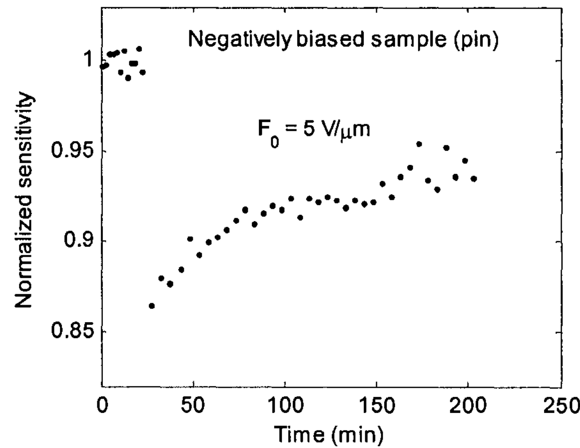

Figure 4.19 Experimental result, $F_0 = 5$ V/μm. Twelve test pulses are radiated before the ghost pulse is applied. The ghost pulse dose is ~1 R.

Using the same approach, test pulses are used initially to measure the initial sensitivity. In this experiment, before the ghost pulse is applied, 12 test pulses are used with a dark-time

of 2 minutes between each two test pulses. After measuring the initial sensitivity, the ghost pulse is applied. The dose of the ghost pulse used for the *p-i-n* sample is ~ 1 R. The first test pulse has been radiated in 5 minutes since the ghost is completed. In the recovery process the dark-time between each two test pulses is 5 minutes. As can be seen from Figure 4.19 the ghosting is not fully recovered after almost three hours. This fact may have the meaning of the presence of other defects across the sample while the ghost is applied. The ghosting is expected to be fully recovered in much longer time than the recovery time.

It is worth-mentioning that the experimental results strongly depend on the operating conditions, and the type of the sample.

In order to do a comparative study on ghosting recovery, other experiment has been done using the same sample but with different electric field F_0 = 10 V/μm. Figure 4.20 shows the result of this experiment. A comparison between this Figure and Figure 4.19 show that the trend of recovery remains almost the same.

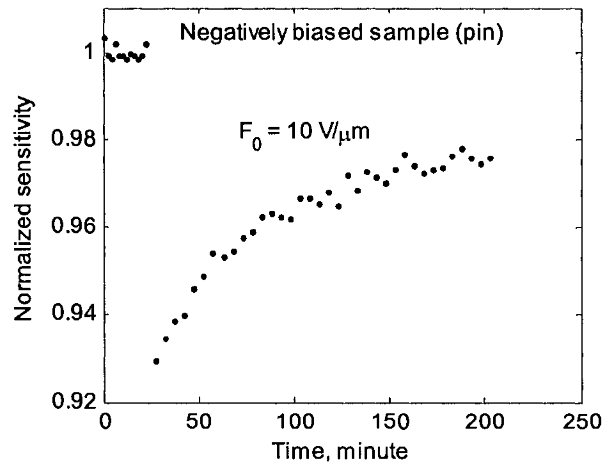

Figure 4.20 Experimental result, F_0 = 10 V/μm. 12 test pulses are radiated before the ghost pulse is applied. The ghost pulse dose is ~1 R.

4.3 Ghosting Recovery (Theoretical Research)

The theoretical ghosting recovery measurement is performed on *p-i-n* structure following the sequence of Figure 3.6. The initial sensitivity is measured using twelve test pulses. The thickness of the sample is 1088 μm. The mobility-lifetimes of carriers in the intrinsic layer are $(\mu_h \tau_{0h})_i = 35\times10^{-6}$ cm^2/V and $(\mu_e \tau_{0e})_i = 3\times10^{-6}$ cm^2/V (measured values). The initial deep trap concentration, $N_0 \approx 3\times10^{18}$ m^{-3} for both holes and electrons in the intrinsic layer. The quantity N_0 in the n and p layers is assumed to be 5×10^{21} m^{-3}. The time interval between each test pulse is 2 minutes. The average photon energy E_{av} is 55 k eV. The numerical results considering effective recombination coefficient ($f = 0.3$) in all three layers in the present model agree well with the experimental data. After obtaining the change in sensitivity for 12 test pulses within first 24 minutes, the ghost pulse is applied. The total exposure for the ghost pulse is 1R. The sensitivity is measured in 5 minute intervals after the ghost is achieved. Fitted values of N_{se} ($=N_{sh}$) and D are 2.5 $\times10^{18}$ m^{-3} and 1.5 R, respectively. Figures 4.21 (a) and 4.21 (b) show the sensitivity recovery as a function of time for a negatively biased *p-i-n* sample at an applied electric field of 5 V/μm , and 10 V/μm respectively. All other parameters in Figure 4.21 (b) are the same as Figure 4.21 (a). The dotted line represents sensitivity recovery considering only hole detrapping, the dot-dashed line shows the sensitivity recovery considering both hole and electron detrapping, and the dashed line represents the sensitivity recovery considering carrier detrapping and the effects of the injected carriers. The open circles show the experimental data and the solid line is the theoretical fit to the experimental data. In the ghosting recovery step, the dark-time between any two test pulses is 5 minutes. The detrapping of holes and electrons are considered with time constants of 10

minutes and 3 hours respectively. The recovery time constant for the meta-stable trap centers is assumed to be 12 hours. It is evident from Figures 4.21 (a) and 4.21 (b) that the ghosting recovery is achieved mainly by the electron release. However, the recombination of the injected holes with the trapped electrons vanishes some of the trapped electrons, which also has a significant effect on the sensitivity recovery process (see the difference between the dotted and dot-dashed lines). The sensitivity is expected to recover fully by resting the sample longer than the recovery time constant of the meta-stable trap centers (the structural relaxation time constant), which is ~15 to 24 hours [47]. The symbols represent the experimental data and the solid lines represent the theoretical fit to the experimental data. The model agrees well with the experimental results.

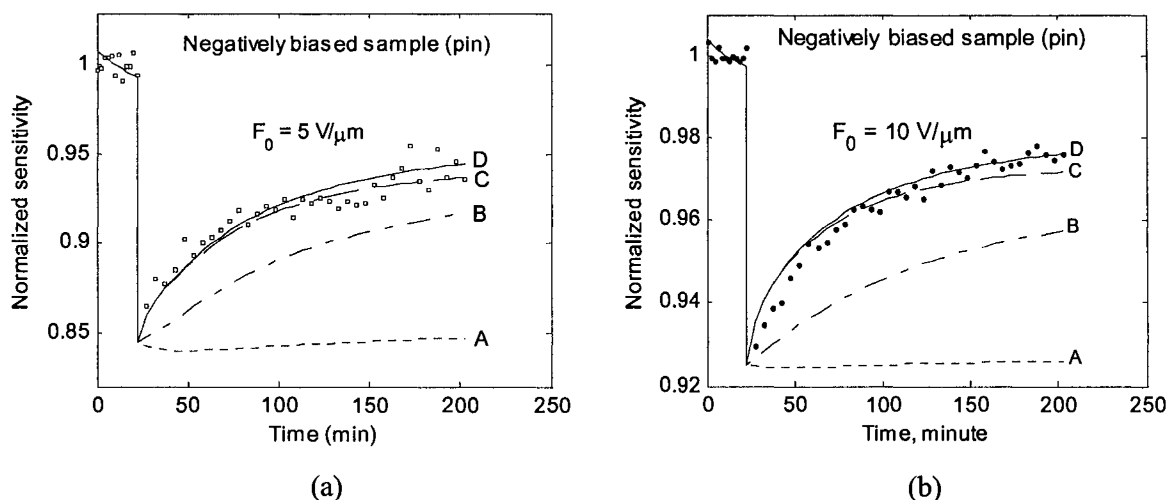

Figure 4.21 Measuring initial sensitivity, applying ghost pulse, and recovery process are shown. In the recovery process the effect of different phenomenon on ghosting recovery is illustrated. A) Shows the effect of hole release on ghosting recovery. B) Shows the effect of hole and electron release. C) Shows the effect of injection plus charge release, and D) is the fit curve including release of new meta-stable deep trap centers. (a) F_0 = 5V/μm, (b) F_0 = 10 V/μm.

As mentioned in section 4.1 the electric fields at both contacts increase with accumulated X-ray exposure. The dark current mainly depends on the contact electric fields as

observed in the recent work by Mahmood *et al.* [61]. Therefore, it is instructive to calculate the change in dark current during the experimental study of ghosting and its recovery. Figure 4.22 (a) and (b) show the electric field distribution and the relative dark current as a function of time at an applied electric field of 10 V/μm. The dark current is calculated by the model described in the recent model [61]. The initial dark current density is the steady state dark current after applying the bias voltage but before any exposure. The initial dark current density is assumed to be 18 pA/cm^2, as measured in the identical samples [61]. During ghosting measurement, the dark current density is calculated at the end of the dark-time and right before the next exposure. There is an increase in dark current during initial test pulses and it settles at a bit higher (almost 5 times of the initial dark current) value quickly. However, the dark current increases very rapidly during the ghosting dose, and it also decreases quite quickly after the ghosting dose. The X-ray generated carriers are trapped in the intrinsic layer. The X-ray generated carriers also recombine with the trapped carriers in the blocking layers (*n* and *p* layers), and temporally reduce the trapped carriers in the blocking layers. The resultant effect is the rapid increase of electric fields at the metal contacts, which enhances the carrier injection. After the ghosting dose, the high injected carriers are readily trapped in the blocking layer, which retains the trapped carriers in the blocking layers and reduces the contact electric field. The slow and monotonous decrease of dark current is due to the carrier releases in the intrinsic layer and the resultant redistribution of electric fields. Note that almost two orders of increase of dark current density during exposure has been observed previously [66]. As such, the present result is consistent with the previous work.

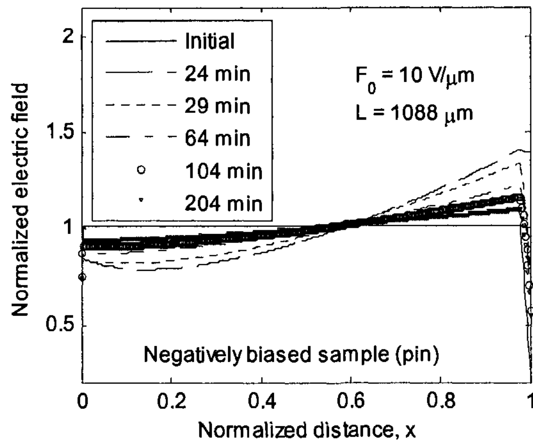

(a)

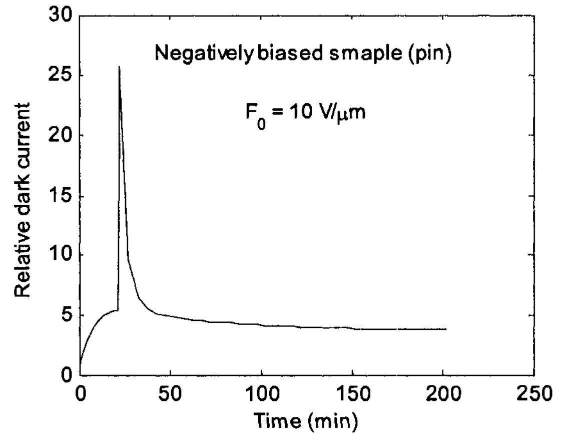

(b)

Figure 4.22 (a) The change in electric field across the photoconductor with time in ghosting recovery process. (b) Relative dark current versus time for the conditions of Figure 4.21 (b).

Chapter 5

Conclusion, Contribution, and Future Work

In this thesis a theoretical/numerical model has been developed for calculating X-ray exposure and time dependent sensitivity reduction (ghosting), dark current, and ghosting recovery for a multilayer amorphous Selenium X-ray detectors. The model considers the effects of carrier transport in all three layers of the detector. Different operating conditions such as bias voltage and polarity (positively biased and negatively biased samples) are also included in the model. In this thesis the performance of such a system is modeled based on the physics of the individual phenomena and the systematic solution of the fundamental physical equations in a photoconductor layer which are; (1) Semiconductor continuity equation, (2) Poisson's equation, and (3) Trapping rate equations. The dynamic model ultimately is useful in developing samples to improve medical image quality and optimize the dosage of radiation for various medical imaging applications.

5.1 Ghosting (Sensitivity Reduction)

A numerical model is developed for calculating the dependence of the X-ray sensitivity of a multilayer a-Se based X-ray medical image detectors on repeated X-ray exposures and exposure history. The present model considers the transport phenomena such as deep trapping of charge carriers, trapped charges due to previous exposures, trap filling effects,

recombination between drifting and oppositely charged trapped carriers, space charge effects, electric field dependent charge carrier generation, X-ray induced new deep trap center generation, detrapping of trapped carriers and the effect of charge injections through the blocking layers with time for multilayer a-Se detectors. The electric field distribution across the photoconductor varies widely depending on operating conditions and exposure history. The electric field at the two ends of the photoconductor decreases due to the trapped holes and electrons in n and p layers respectively. The relative and absolute sensitivity have more reduction in multilayer photoconductor due to the less EHP generation at the radiation receiving side. The blocking layers have more effect in positively biased sample compared to a negatively biased sample. The relative sensitivity decreases with increasing accumulated X-ray exposure. The most important role of the dark current on ghosting is the trapping of injected carriers in the blocking layers which compensate the loss of trapped carriers during exposures. The amount of dark current also increases dramatically within the first few exposures and the increase of dark current will decrease with time and will be saturated after some times. The amount of ghosting is examined as a function of initial electric field. The more the electric field is the less the amount of ghosting will be. The concentration of deep trapped carriers in the blocking layers has been estimated with respect to the initial dark current obtained by the dark current model. The comparison of the numerical model with the experimental data shows that the recombination between trapped and the oppositely charged drifting carriers, electric field dependent charge carrier generation and X-ray induced new deep trap centers are mainly responsible for the sensitivity reduction in biased a-Se- based X-ray detectors. It is expected that the ghosting phenomenon may also be observed in other

photoconductive (*e.g.* HgI_2, CdZnTe, and PbI_2) detectors although it has not yet been measured.

5.2 Ghosting Recovery

The numerical model for ghosting is expanded in order to study natural ghosting recovery. The principals of recovery model are based on the ghosting model. Ghosting recovery model is examined for a negatively biased sample. In the recovery process the sample is rested for almost 3 hours and within this time the ghost is mostly recovered. The sensitivity in the rested sample is recovered mainly by the carrier detrapping and the recombination of the injected carriers with the existing trapped carriers. The electric fields at the metal contacts decrease with time in ghosting recovery process which leads to the reduction of dark current. The rate of the reduction of the dark current during recovery stage is very high initially and the reduction rate decreases with time. The sensitivity is expected to recover almost fully by resting the sample longer than the recovery time constant of the meta-stable trap centers (the structural relaxation time constant), which is in the time scale of 15–24 hours. The numerical result shows a very good agreement with the experimental data.

It should be mentioned that both the ghosting and recovery studies have been followed by experimental studies as well.

5.3 Contributions

The author contributed to the following original developments:

- A theoretical model has been developed by incorporating carrier transport in all three layers of the multilayer a-Se sample.

- Charge injection is included into the model so as to study the effect of dark current on charge collection and charge distributions across a multilayer sample.
- Natural ghosting recovery is theoretically studied by extending the numerical model. Possible different phenomena and their contributions to the ghosting recovery were studied theoretically for the first time.
- Useful experiments and measurements have been carried out to study the ghosting and its recovery in a-Se sample. The results were subjected to an investigation in terms of consistency with physical conceptions and theoretical model.

5.4 Suggestions and Future Work

Amorphous Se is one of the interesting materials in terms of unpredictable/uncertain behaviours that it has been shown so far and it still attracts researchers' attentions. For instance, the trapping and recombination mechanisms (the two most important phenomena known so far that control the ghosting) are still debatable.

Furthermore, the developed numerical ghosting model has examined the sensitivity reduction in multilayer a-Se based X-ray detector, yet there are other common photoconductors (HgI_2, CdZnTe, and PbI_2) used in the medical X-ray image detectors. Both the ghosting and its recovery model can be implemented for the above multilayer photoconductors based upon the availability of the experimental data. The behavior of dark current with accumulated X-ray exposures and time can also be as systematically studied as what has been done in this thesis.

Ghosting could also be erased by applying some external means. For example, applying light after each exposure may also erase ghosting. The illuminated light can create EHPs inside the sample and these created charges may recombine with the oppositely charged

trapped carriers and recover the sensitivity. It is instructive to study the appropriate wavelength of light within visible or near visible spectra to eliminate ghosting. Such investigations would be interesting to be followed on different types of samples (*n-i*, *n-i-p*, *p-i-n*, *i*) with different thicknesses of different layers. This study may also help to investigate the exact physics of ghosting in this class of detectors.

REFERENCES

[1] J. A. Rowlands and S. O. Kasap "Amorphous semiconductors usher in digital x-ray imaging," *Physics Today*, **50**, pp. 24-30, and references therein, (1997).

[2] S. O. Kasap and J. A. Rowlands, "Direct conversion flat panel X-ray image detectors," *IEE Proc.-CDS*, **149**, pp. 85-96, (2002).

[3] J. A. Rowlands and J. Yorkstone, "Flat panel detectors for digital radiography," in Handbook of Medical Imaging, Vol. 1, edited by J. Beutel, H. L. Kundel and R. L. Van Metter (SPIE press Washington), chapter 4 and references therein, (2000).

[4] G. Harrel, MS Chotas, James T. Dobins, and Carl E. Ravin MD, "Principles of Digital Radiography with Large-Area, Electronically Readable, Detetcors: A Review of the Basics," *RSNA Radiology*, **210**, pp. 595-599, (1999).

[5] D. C. Hunt, O. Tousignant, and J. A. Rowlands, "Evaluation of the imaging properties of an amorphous selenium- based flat panel detector for digital fluoroscopy," *Med. Phys.* **31**, pp. 1166-1175, (2004).

[6] M. Choquette, H. Rougeote, J. Martin, L. Laperriere, Z. Shukri, and B. Polischuk, "Direct Selenium X-ray detector for fluoroscopy, R&F, and Radiography," *Proc. SPIE*, **3977**, pp. 128-136, (2000).

[7] B. Polischuk, H. Rougeote, K. Wong, A. Debrie, E. Poliquin, M. Hansrol, J. P. Martin, T. T. Truong, M. Choquette, L. Laperriere, and Z. Shukri, "Direct conversion detector for digital mammography," *Proc. SPIE*, **3659**, pp. 417-425, (1999).

[8] E. Samei and M. J. Flynn, "An experimental comparison of detector performance for direct and indirect digital radiography systems," *Med. Phys.*, **30**, pp. 608-622, (2003).

[9] R. S. Saunders Jr., E. Samei, and C. Hoeschen, "Impact of resolution and noise characteristics of digital radiographic detectors on the detectability of Lung nodules," *Med. Phys.*, **30**, pp. 1603-1613, (2004).

[10] M. Z. Kabir, E. V. Emelianova, V. I. Arkhipov, M. Yunus, S. O. Kasap, and G. Adriaenssens, "The effect of large signals on charge collection in radiation detectors: Application to amorphous selenium detectors," *J. Phys. D: Appl. Phys.*, **99**, (2006).

[11] S. O. Kasap, "Photoreceptors: the selenium alloys," *in HandBook of Imaging Materials*, edited by A. S. Diamond (Marcel Dekker, New York), pp. 329-372, (1991).

[12] S. O. Kasap and J. A. Rowlands, "X-ray photoconductors and stabilized a-Se for direct conversion digital flat panel x-ray image detectors," in Optoelectronics & Photonics: Principles and Practices, S.O. Kasap, (Prentice-Hall, Upper Saddle River, New Jersey), in CDROM, (2001).

[13] M. Z. Kabir, M. Yunus, S.O. Kasap, O. Tousignant, H. Mani, and P. Gauthier, "Sensitivity of stabilized a-Se based Xray photoconductors," *Current Appl. Phys.*, **6**, pp. 393-398, and references therein, (2006).

[14] S. Steciw, T. Stanescu, S. Rathee, and B.G. Fallone, "Sensitivity reduction in biased amorphous selenium photoconductors," *J. Phys. D: Appl. Phys.,* **35**, pp. 2716-2722, (2002).

[15] A. W. Rau, L. Bakueva, and J. A. Rowlands, "The x-ray time of flight method for investigation of ghosting in amorphous selenium-based flat panel medical x-ray imagers," *Med. Phys.*, **32**, pp. 3160-3177, (2005).

[16] G. Belev and S. O. Kasap, "Reduction of the dark current in stabilized a-Se based X-ray detectors," *J. Non-Cryst. Solids,* **352**, pp. 1616-1620, (2006).

[17] S. O. Kasap and G. Belev, "Progress in the science and technology of direct conversion X-ray image detectors: The development of a double layer a-Se based detector," *J. Opt. & Adv. Mat.*, **9**, pp. 1-10, and references therein, (2007).

[18] J. M. Boone, "X-ray production, interaction, and detection in diagnostic imaging," in Handbook of Medical Imaging, Vol. 1, edited by J. Beutel, H. L. Kundel and R. L. Van Metter (SPIE Press, Washington), chapter 1 and references therein, (2000).

[19] http://physics.nist.gov/PhysRefData/

[20] S.O. Kasap and J.A. Rowlands, "Review: X-ray photoconductors and stabilized a-Se for direct conversion digital flat-panel x-ray image detectors," *Journal of Materials Science: Materials in Electronics,* **11**, pp. 179-198, (2000).

[21] M. Abkowitz, "Density of states in a-Se from combined analysis of xerographic potentials and transient transport data," *Philosophical Magazine Lett.*, **58**, pp. 53–57, (1988).

[22] B. J. Fogal, "Electronic Transport Properties of Stabilized Amorphous Selenium X-ray Photoconductors," Doctoral Thesis, Department of Electrical Engineering, University of Saskatchewan, Saskatoon, Canada, (2005).

[23] S. O. Kasap and C. Juhasz, "Time-of-flight drift mobility measurements on chlorine doped amorphous selenium films," *J. Phys. D: Applied Physics*, **33**, pp. 703-720, (1985).

[24] H.-Z. Song, G. J. Adriaenssens, E. V. Emelianova, and V. I. Arkhipov, "Distribution of gap states in amorphous selenium thin films," *Phys. Rev. B.*, **59**, pp. 10607-10613, (1999).

[25] S. O. Kasap and J. A. Rowlands, "Direct-conversion flat panel x-ray image sensors for digital radiography," *Proc. IEEE*, **90**, pp. 591-604, (2002).

[26] S. O. Kasap, V. Aiyah, B. Polischuk, A. Bhattacharyya, and Z. Liang, "Deep-trapping kinematics of charge carriers in amorphous semiconductors: A theoretical and experimental study," *Phys. Rev. B*, **43**, pp. 6691-6705, (1991).

[27] K. Koughia, Z. Shakoor, S. O. Kasap, and J. M. Marshall, "Density of localized electronic states in a-Se from electron time-of-flight photocurrent measurements," *J. Appl. Phys.*, **97**, 033706, (2005).

[28] I. M. Blevis, D. C. Hunt, and J. A. Rowlands, "Measurement of X-ray photogeneration in amorphous selenium," *J. Appl. Phys.*, **85**, pp. 7958-7963, (1999).

[29] M. F. Stone, W. Zhao, and B. V. Jacak, P.O'Conner, B. Yu, and P. Rehak, "The x-ray sensitivity of amorphous selenium for mammography," *Med. Phys.*, **29**, pp. 319-324, (2002).

[30] S. O. Kasap, M. Z. Kabir, and J. A. Rowlands, "Recent advances in X-ray photoconductors for direct conversion X-ray image sensors," Current Applied Physics, vol. **6**, pp. 288-292, (2006).

[31] S. O. Kasap, "X-ray sensitivity of photoconductors: application to stabilized a-Se," *J. Phys. D: Applied Physics*, **33**, pp. 2853-2865, (2000).

[32] W. Que and J. A. Rowlands, "X-ray photogeneration in amorphous selenium: Geminate versus columnar recombination," *Phys. Rev.*, B, **51**, pp. 10500–10507, (1995).

[33] B. Polischuk, Z. Shukri, A. Legros, and H. Rougeot, "Selenium direct converter structure for static and dynamic x-ray detection in medical imaging," *Proc. SPIE*, **3336**, pp. 494-504, (1998).

[34] M. Kastner and D. Adler, "Valence-Alternation Model for Localized Gap States in Lone-Pair Semiconductors," *Phys. Rev. Lett.*, **37**, pp. 1504-1507, (1976).

[35] D. K. Biegelsen and R. A. street, "Photoinduced Defects in Chalcogenide Glasses," *Physical Review Lett.*, **44**, pp. 803-806, (1980).

[36] M. Abkowitz and R. C. Enck, "Photoenhanced metastable deep trapping in amorphous chalcogenides near room temperature," *Phys. Rev. B*, **27**, pp. 7402-7411, (1983).

[37] C. Haugen and S. O. Kasap, "Langevin recombination of drifting electrons and holes in stabilized a-Se (Cl-doped a-Se:0.3% As)," *Philosophical Magazine,* **71**, pp. 91-96, (1995).

[38] S. O. Kasap, B. Fogal, M. Z. Kabir, R. E. Johanson, and S. K. O'Leary, "Recombination of drifting holes with trapped electrons in stabilized a-Se photoconductors: Langevin recombination," *Appl. Phys. Lett.*, **84**, pp. 1991-1993, (2004).

[39] M. Yunus, M. Z. Kabir, and S. O. Kasap, "Sensitivity reduction mechanisms in amorphous selenium photoconductive x-ray image detectors," *Appl. Phys. Lett.*, **85**, pp. 6430-6432, (2004).

[40] A. V. Kolobov, M. Kondo, H. Oyanagi, A. Matsuda, and K. Tanaka, "Negative correlation energy and valence altmation in amorphous selenium: an in situ optically induced ESR study," *Phys. Review B,* **58**, pp. 12004-12010, (1998).

[41] A. V. Kolobov (ed.), "Photo-induced metastability in amorphous semiconductors," (Wiley-Vch, Weinheim) chapter 3, (2003).

[42] Fritzsche H., "The origin of reversiile and ineversiile photostructural changes in chalcogenide glasses," *Philosophical Magazine B*, **68**, pp. 561-572, (1993).

[43] U. Schiebel, T. Buckremer, G. Frings, and P. Quadfling, "Deep trapping and recombination in a-Se:As X-ray sensitive photoreceptors," *J. Non-Cryst. Solids,* **115**, pp. 216-218, (1989).

[44] S. O. Kasap, V. Aiyah, A. Baillie, and A. G. Leiga, "X-ray Induced Hole Trapping in Electroradiographic Plates," *J. Appl. Phys.*, **69**, pp. 7087-7096, (1991).

[45] M. Nesdoly, "X-ray sensitivity and x-ray induced charge transport changes in stabilized a-Se films," Doctoral Thesis, Department of Electrical Engineering, University of Saskatchewan, Saskatoon, Canada, (2000).

[46] R. A. Street, "Recombination in amorphous semiconductors," *Phys. Rev. B*, **17**, pp. 3984-3995, (1978).

[47] C. Allen, G. Belev, R. Johanson, and S. O. Kasap, "Relaxation of electrical properties of stabilized amorphous selenium based photoconductors," J. Non-Crystalline Solids, 354, 2711, (2008).

[48] Y. Nemirovsky, A. Ruzin, G. Asa, and J. Gorelik, "Study of the charge collection efficiency of CdZnTe radiation detectors," *J. Electron. Mater.*, **25**, pp. 1221-1231, (1996).

[49] M. Z. Kabir and S. O. Kasap, "Sensitivity of x-ray photoconductors: Charge trapping and absorption-limited universal sensitivity curves," *J. Vac. Sci. Tech. A,* **20**, pp. 1082-1086, (2002).

[50] R. A. Street, S. E. Ready, K. Van Schuylenbergh, J. Ho, J. B. Boyec, P. Nylen, K. Shah, L. Melekhov, and H. Hermon, "Comparison of PbI2 and HgI2 for direct detection active matrix x-ray image sensors," *J. Appl. Phys.*, **91**, pp. 3345-3355, (2002).

[51] M. Z. Kabir and S. O. Kasap, "Charge collection and absorption-limited sensitivity of x-ray photoconductors: Applications to a-Se and HgI2," *Appl. Phys. Lett.*, **80**, pp. 1664-1666, (2002).

[52] C. A. Klein, "Bandgap dependence and related features of radiation ionization energies in semiconductors," *J. Appl. Phys.*, **39**, pp. 2029-2038, (1968).

[53] W. Zhao, G. DeCrescenzo, and J. A. Rowlands, "Investigation of lag and ghosting in amorphous selenium flat-panel x-ray detectors," *Proc. SPIE,* **4682**, pp. 9-20, (2002).

[54] M. Abkowitz and R. C. Enck, "Photoenhanced metastable deep trapping in amorphous chalcogenides near room temperature," Phys. Rev. B, 27, pp. 7402-7411, (1983).

[55] U. Schiebel, T. Buckremer, G. Frings, and P. Quadfling, "Deep trapping and recombination in a-Se:As X-ray sensitive photoreceptors," *J. Non-Cryst. Solids,* **115**, pp. 216-218, (1989).

[56] S. O. Kasap, V. Aiyah, A. Baillie, and A. G. Leiga, "X-ray induced hole trapping in electroradiographic plates," *J. Appl. Phys.*, **69**, pp. 7087-7096, (1991).

[57] M. Z. Kabir, **F. Manouchehri**, S. A. Mahmood, V. K. Devabhaktuni, O. Tousignant, H. Mani, J. Greenspan, and P. Botka, "Modeling of dark current and ghosting in multilayer amorphous selenium X-ray detectors," *Proc. SPIE*, **6913**, (2008).

[58] C. Haugen and S. O. Kasap, "Langevin recombination of drifting electrons and holes in stabilized a-Se (Cl-doped a-Se: 0.3% As)," *Philosophical Magazine,* **71**, pp. 91-96, (1995).

[59] S. O. Kasap, B. Fogal, M. Z. Kabir, R. E. Johanson, S. K. O'Leary, and S. O. Kasap, "Recombination of drifting holes with trapped electrons in stabilized a-Se photoconductors: Langevin recombination," *Appl. Phys. Lett.*, **84**, pp. 1991-1993, (2004).

[60] M. Z. Kabir, M. Yunus, and S. O. Kasap, "Dependence of x-ray sensitivity of direct conversion x-ray detectors on x-ray exposure and exposure history," *Proc. SPIE – Int. Soc. Opt. Eng.,* **5368**, pp. 170-176, (2004).

[61] S. A. Mahmood, M. Z. Kabir, O. Tousignant, H. Mani, J. Greenspan, and P. Botka, "Dark current in multilayer a-Se x-ray imaging detectors," *Appl. Phys. Lett.*, **92**, (2008).

[62] W. Shockley, "Currents to conductors induced by a moving point charge," *J. Appl. Phys.*, **9**, pp. 635-636, (1938).

[63] A. E. Iverson and D. L. smith, "Mathematical modeling of photoconductor transient response," *IEEE Trans. Electron Devices,* **ED-34**, pp. 2098-2107, (1987).

[64] K. C. Kao and W. Hwang, "Electrical transport in Solids," Pergamon press, London, chapter 5, (1981).

[65] B. Zhao and W. Zhao, "Temporal performance of amorphous selenium mammography detectors," *Med. Phys.*, **32**, pp. 128-136, (2005).

[66] B. Fogal, R. E. Johanson, G. Belev, S. O'Leary, and S. O. Kasap, "X-ray induced effects in stabilized a-Se x-ray photoconductors," *J. Non-Crystalline Solids*, **299-302**, pp. 993-997, (2002).